

## **Grid-free compressive mode extraction**

Yongsung Park, Peter Gerstoft, and Woojae Seong

Citation: [The Journal of the Acoustical Society of America](#) **145**, 1427 (2019); doi: 10.1121/1.5094345

View online: <https://doi.org/10.1121/1.5094345>

View Table of Contents: <https://asa.scitation.org/toc/jas/145/3>

Published by the [Acoustical Society of America](#)

---

### **ARTICLES YOU MAY BE INTERESTED IN**

[Gap-filling method for suppressing grating lobes in ultrasound imaging: Theory and simulation results](#)  
The Journal of the Acoustical Society of America **145**, EL236 (2019); <https://doi.org/10.1121/1.5094337>

[Three dimensional photoacoustic tomography in Bayesian framework](#)  
The Journal of the Acoustical Society of America **144**, 2061 (2018); <https://doi.org/10.1121/1.5057109>

[Generalized optical theorem for an arbitrary incident field](#)  
The Journal of the Acoustical Society of America **145**, EL185 (2019); <https://doi.org/10.1121/1.5092581>

[Steerable sparse linear array design based on compressive sensing with multiple measurement vectors](#)  
The Journal of the Acoustical Society of America **145**, 1212 (2019); <https://doi.org/10.1121/1.5092212>

---

# Grid-free compressive mode extraction

Yongsung Park,<sup>1,a)</sup> Peter Gerstoft,<sup>1</sup> and Woojae Seong<sup>2,b)</sup>

<sup>1</sup>Scripps Institution of Oceanography, University of California San Diego, La Jolla, California 92093-0238, USA

<sup>2</sup>Department of Naval Architecture and Ocean Engineering, Seoul National University, Seoul, 08826, Republic of Korea

(Received 3 September 2018; revised 21 February 2019; accepted 22 February 2019; published online 20 March 2019)

A grid-free compressive sensing (CS) based method for extracting the normal modes of acoustic propagation in the ocean waveguide from vertical line array (VLA) data is presented. Extracting the normal modes involves the estimation of mode horizontal wavenumbers and the corresponding mode shapes. Sparse representation of the waveguide propagation using modes at discrete horizontal wavenumbers enables CS to be applied. Grid-free CS, based on group total-variation norm minimization, is adopted to mitigate the issues of the wavenumber search grid discretization in the conventional CS. In addition, the suggested method can process multiple sensor data jointly, which improves performance in estimation over single sensor data processing. The method here uses data on a VLA from a source at several ranges, and processes the multiple sensor data at different depths jointly. The grid-free CS extracts the mode wavenumbers and shapes even with no *a priori* environmental knowledge, a partial water column spanning array data, and without the mode orthogonality condition. The approach is illustrated by numerical simulations and experimental SWellEx-96 (shallow water evaluation cell experiment 1996) data. © 2019 Acoustical Society of America.

<https://doi.org/10.1121/1.5094345>

[ZHM]

Pages: 1427–1442

## I. INTRODUCTION

Normal mode methods have been widely used for acoustic wave problems, and the normal mode structure of an ocean waveguide describes the propagation of underwater sound.<sup>1</sup> The problem of normal mode extraction from vertical line array (VLA) data is to resolve the acoustic signals into discrete normal modes and estimate the mode horizontal wavenumbers associated with the discrete modes and corresponding depth-dependent mode shape functions. We formulate the normal mode extraction as a sparse signal reconstruction problem, and propose a compressive sensing (CS) for recovering the sparse mode wavenumbers and mode amplitudes. The proposed method uses data on a VLA from a source at several ranges and processes multiple sensor data at different depths jointly. The recovered mode amplitudes at several depths along the VLA bring forth the corresponding mode shapes. The extracted modes offer a wide range of applications from source localization, including matched mode processing,<sup>2–4</sup> matched field processing,<sup>5,6</sup> and time reversal mirror,<sup>7,8</sup> to inversion,<sup>9,10</sup> tomography,<sup>11,12</sup> and marine mammal localization.<sup>13</sup>

Traditional approaches for extracting modes involve matched mode or mode filtering methods,<sup>14,15</sup> which require *a priori* information about the environment to generate the modeled modes that match the measured data, and these methods tend to be highly sensitive to the environmental

mismatch. To determine the modes from measured acoustic data alone without environmental information, singular value decomposition (SVD) is applied using that the acoustic pressure field is a superposition of normal modes.<sup>16–19</sup> This method is based on the premise that the eigenvectors of the sample covariance matrix (SCM) of the pressure field measured on a VLA correspond to the mode shapes. This premise requires the depth-dependent mode shapes be orthonormal, but this is not trivial. The orthonormality requires that the VLA perfectly spans the waveguide, which consists of a layer and bottom layers. To overcome the orthonormality constraint, it is suggested to isolate the modes in the frequency-wavenumber domain and extract the mode shapes individually with SVD using the isolated mode wavenumbers.<sup>18,19</sup> The method introduces a frequency-wavenumber modal dispersion curve isolation for decoupling the modes in the SCM, but for low order modes having closely located mode wavenumbers, the decoupling fails. Other approaches for isolating modes are proposed in the time-frequency domain,<sup>13,20,21</sup> and these methods require impulsive source and selection of an appropriate time origin, which is dependent on the mode chosen. Note that, these methods are based on the fact that the modes are separated in either the frequency-wavenumber domain or time-frequency domain, which means that the modes have a sparse representation in these domains. Here, we utilize the sparse representation of the modes in the frequency-wavenumber domain.

For a sufficiently large range sample aperture, the modes show distinct dispersion curves in the frequency-wavenumber domain.<sup>22</sup> When considering the wavenumber spectrum at one frequency, the spectrum has non-zero components at the mode wavenumbers, so it can be considered

<sup>a)</sup>Also at: Department of Naval Architecture and Ocean Engineering, Seoul National University, Seoul, 08826, Republic of Korea.

<sup>b)</sup>Also at: Research Institute of Marine System Engineering, Seoul National University, Seoul, 08826, Republic of Korea. Electronic mail: wseong@snu.ac.kr

as a sparse signal. As a result, estimating the wavenumbers and the corresponding mode amplitudes is a sparse signal reconstruction problem. CS, which promotes sparse solutions, is a method for solving such sparse signal reconstruction problems.<sup>23–25</sup> CS has been applied in many estimation problems and has shown superior performance compared to existing techniques.<sup>22,26–34</sup> In acoustics, CS based wavenumber estimation has shown its ability to recover the dispersive behavior of the wavenumber with great accuracy using few observations.<sup>22,32–35</sup>

A problem with the conventional CS is basis mismatch,<sup>36,37</sup> which occurs when the actual components in a continuous parameter space do not fall on the discretized search grid. The basis mismatch has significant drawbacks. First, when the basis mismatch occurs, the signal might not often be sparsely represented using a discrete grid. Second, it becomes difficult analyzing conventional CS performance since the coherence among the grid points becomes high for a dense grid. Third, although finer grids may mitigate the basis mismatch and improve the reconstruction error, very fine grids can lead to numerical instability issues.<sup>26,36,38</sup> This concern leads to the need for grid-free models, and to cope with basis mismatch, grid-free CS techniques, which directly promote sparsity in the continuous parameter space, have been proposed.<sup>38,39</sup> Grid-free CS has been applied in acoustics, and has been shown to overcome basis mismatch with its superior estimation performance.<sup>40–43</sup>

Multiple measurement processing, which jointly processes all the multiple measurements and estimates the parameter of interest, is an intuitive way to improve the estimation performance. For beamforming, multiple snapshot CS beamforming outperforms conventional high-resolution methods and single snapshot CS beamforming.<sup>27,28</sup> Similarly, grid-free CS has been developed for the multiple measurement processing model,<sup>44–48</sup> and in the beamforming problem, multiple snapshot grid-free CS beamforming outperforms existing methods.<sup>49</sup>

The normal mode extraction problem is here formulated as a sparse signal reconstruction problem with multiple measurements and solved with grid-free CS. Let us recall the wavenumber and corresponding mode amplitude estimation at a single frequency from VLA data. In this paper, the experimental setup involves a source and a VLA, and the source is recorded by the VLA for many ranges. For each VLA sensor, a wavenumber spectrum is extracted from data measured at all source-receiver ranges, and this wavenumber spectrum is expressed as a sparse signal. The sparse signal at each depth has non-zero components at the same wavenumbers, but different amplitudes at these mode wavenumbers. In this setup, the multiple measurements are considered as multiple sensor data at different depths.

Thus, we suggest a technique for estimating jointly the mode wavenumbers and the corresponding mode amplitudes. The technique can process multiple sensor data jointly to estimate the mode wavenumbers shared by multiple sensor data at different depths, and can estimate the mode wavenumbers in a grid-free manner and the corresponding mode amplitudes. Since the VLA sensors have different depths, each set of mode amplitudes sharing the

same mode wavenumber constructs the corresponding depth-dependent mode shape.

To formulate the mode extraction as grid-free CS with multiple measurement processing framework, we utilize group total-variation (gTV) norm<sup>44,49</sup> as a continuous measure for enforcing sparsity over multiple measurements (measurement matrix). gTV norm is an extension of total-variation (TV) norm,<sup>39–41</sup> which is a continuous measure for enforcing sparsity but for single measurement vector. The suggested group total-variation norm minimization (gTVNM) based mode extraction technique locates common non-zero components across sparse signals in the wavenumber domain and recovers their amplitudes. Therefore, the reconstructed signal is a set of sparse signals, which have common non-zero components at the mode wavenumbers with amplitudes as the mode amplitudes, constructing the depth-dependent mode shapes.

With sparse representation of the pressure field as a superposition of discrete normal modes, we introduce CS. To overcome the basis mismatch issues for conventional CS and process multiple sensor data, we present grid-free CS, which can jointly cover the multiple measurements. Grid-free CS has been applied to beamforming in underwater acoustics,<sup>40,41</sup> but has not been applied to the normal mode extraction. The grid-free CS mode extraction technique does not require the modes satisfy the orthogonality condition, so grid-free CS provides accurate reconstruction results even with a partial water column spanning array, as well as in situations when the mode shapes are coherent.

In this paper, vectors are represented by bold lowercase letters and matrices by bold uppercase letters. We use “ $T$ ” and “ $H$ ” to denote transpose and conjugate transpose, respectively. In addition, we use continuous variable in italic, like  $X$  and  $k_r$ , and operator  $\mathcal{F}_N$ , which maps the continuous variable to the  $N$ -dimensional vector.

## II. GRID-FREE CS MODE EXTRACTION

### A. Normal mode theory applied to the VLA pressure field

This section derives an expression for the pressure field measured over a VLA using normal mode theory. We use the frequency-time Fourier transform pair,

$$\begin{aligned} p(f) &= \int_{-\infty}^{\infty} p(t)e^{-j2\pi ft} dt, \\ p(t) &= \int_{-\infty}^{\infty} p(f)e^{j2\pi ft} df, \end{aligned} \quad (1)$$

leading the sign of the exponent opposite to Ref. 1. Given the transform pair and the corresponding radiation condition, we can take the Hankel function of the second kind to describe the pressure field with normal mode theory. Consider a single frequency  $\omega_0$  point source at depth  $z_s$  in a range-independent shallow ocean waveguide whose field is measured by a single receiver at  $(z = z_r, r = 0)$  after propagation over a range  $r$ . Normal mode theory describes the pressure field  $p(\omega_0, z_r, r)$ , using the asymptotic approximation of the Hankel function, Eq. (5.14) of Ref. 1, but taking the Hankel function of the second kind,

$$p(z_r, r) \approx Q \sum_{k=1}^K \left( \Psi_k(z_s) \Psi_k(z_r) \frac{e^{-jk_{c,k}r}}{\sqrt{k_{c,k}r}} \right), \quad (2)$$

where  $Q = S(\omega_0)e^{j\pi/4}/\sqrt{8\pi\rho(z_s)}$ ,  $K$  is the number of propagating modes,  $k_{c,k} = k_{r,k} - jk_{i,k}$  is the complex  $k$ th mode horizontal wavenumber with real and imaginary parts,  $k_{r,k}$  and  $k_{i,k}$ , and  $\Psi_k(z)$  is the corresponding depth-dependent mode shape. The quantity  $S$  is the source spectrum and  $\rho(z_s)$  represents the water density at the source. The experimental setup required for the grid-free CS mode extraction technique consists of an  $M$  element VLA at depths,  $z_1, \dots, z_M$  and a source at depth  $z_s$ , as shown in Fig. 1. The sound pressure at each hydrophone is recorded over a time interval with source-receiver ranges,  $r_1, \dots, r_N$ . We assume that the processed single frequency originates from one source in the far-field, such that the discrete modes propagate to long ranges,  $k_{r,k} \gg k_{i,k}$  ( $k_{i,k}$  represents attenuation).

In this paper, we focus on the real part, i.e.,  $k_{c,k} = k_{r,k}$ . The VLA pressure field  $\mathbf{P} \in \mathbb{C}^{M \times N}$  is described by

$$\begin{aligned} \mathbf{P} &= \begin{bmatrix} p(z_1, r_1) & \cdots & p(z_1, r_N) \\ \vdots & \ddots & \vdots \\ p(z_M, r_1) & \cdots & p(z_M, r_N) \end{bmatrix} \\ &= \sum_{k=1}^K \begin{bmatrix} \Psi_{k,1} c_{k,1} e^{-jk_{r,k}r_1} & \cdots & \Psi_{k,1} c_{k,N} e^{-jk_{r,k}r_N} \\ \vdots & \ddots & \vdots \\ \Psi_{k,M} c_{k,1} e^{-jk_{r,k}r_1} & \cdots & \Psi_{k,M} c_{k,N} e^{-jk_{r,k}r_N} \end{bmatrix} \\ &= \sum_{k=1}^K \Psi_k \tilde{\mathbf{c}}_k^\top, \end{aligned} \quad (3)$$

where  $\Psi_{k,m} = \Psi_k(z_m)$ ,  $\Psi_k = [\Psi_{k,1}, \dots, \Psi_{k,M}]^\top$  are the mode shapes at the receiver,  $c_{k,n} = Q\Psi_k(z_s)/\sqrt{k_{r,k}r_n}$  and  $\tilde{\mathbf{c}}_k = [c_{k,1} e^{-jk_{r,k}r_1}, \dots, c_{k,N} e^{-jk_{r,k}r_N}]^\top$ . The goal of mode extraction is to estimate  $K$  horizontal wavenumbers in the wavenumber domain, determined by  $N$  range data. Based on the estimated horizontal wavenumbers, the corresponding mode shapes are computed.

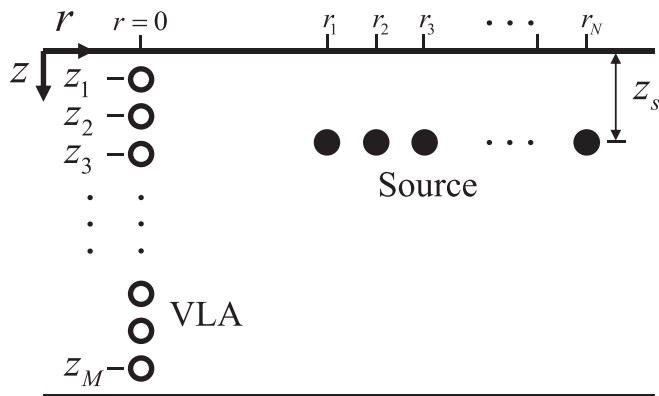


FIG. 1. Experimental setup. A VLA composed of  $M$  hydrophones (open circles) located at range  $r=0$  records the sound pressure from a source (closed circles) at many ranges,  $r_1, \dots, r_N$ , and depth  $z_s$ .

## B. System framework for grid-free CS mode extraction

In this section, the measurement for grid-free CS mode extraction is described. Consider the pressure field  $\mathbf{P} \in \mathbb{C}^{M \times N}$  recorded by a VLA composed of  $M$  hydrophones with  $N$  source-VLA ranges with  $K$  propagating modes, Eq. (3). The  $N$  ranges are uniformly sampled with sampling interval  $R_s$ , i.e.,  $\mathbf{r} = [r_1, \dots, r_N]^\top = [r_1, \dots, r_1 + (N-1)R_s]^\top$ , and time synchronization corresponding to the source-VLA ranges is required. To reduce range dependence in  $c_{k,n}$ , assuming cylindrical spreading, we scale the measurement matrix  $\mathbf{Y} = \mathbf{P}\mathbf{R}$ , where  $\mathbf{R} = \text{diag}(\sqrt{r_1}, \dots, \sqrt{r_N})$ . In our grid-free CS mode extraction framework, the measurement matrix  $\mathbf{Y}$  takes the form of

$$\begin{aligned} Y_{m,n} &= \sum_{k=1}^K x_{m,k} e^{-jk_{r,k}r_n} + E_{m,n}, \\ m &= 1, \dots, M, \quad n = 1, \dots, N, \end{aligned} \quad (4)$$

where  $x_{m,k} = Q\Psi_k(z_s)\Psi_{k,m}/\sqrt{k_{r,k}}$  and  $\mathbf{E} \in \mathbb{C}^{M \times N}$  is additive Gaussian noise. Formally, grid-free CS mode extraction reconstructs a sparse signal, which has its support as the wavenumbers,  $\{k_{r,1}, \dots, k_{r,K}\}$  with its amplitude related to the  $k$ th mode amplitude at the  $m$ th sensor,  $x_{m,k} = Q\Psi_k(z_s)\Psi_{k,m}/\sqrt{k_{r,k}}$ .

For single sensor data  $\mathbf{y}_{m,:} = [y_{m,1}, \dots, y_{m,N}] \in \mathbb{C}^N$ , corresponding to the  $m$ th row of the matrix  $\mathbf{Y}$ , which is the received data at the  $M$ th single sensor of the VLA, is used as the input measurement vector. The grid-free CS problem then becomes the total-variation norm minimization (TVNM) problem, which is a single measurement vector processing scheme. From single sensor data processing, it is possible to obtain the wavenumbers from support of a sparse signal and the mode amplitudes from amplitudes of the sparse signal. The mode shapes are obtained with additional sensor data at several depths. The gTVNM, which is a multiple measurement vector processing scheme, can process multiple sensor data jointly from the full input measurement matrix. The multiple measurement vector processing improves performance in estimation over the single measurement vector processing.<sup>44,49</sup> gTVNM based mode extraction scheme improves support detection, which is the wavenumber estimation, and estimates the mode amplitudes at several depths, which construct the depth-dependent mode shapes.

In the gTVNM framework, the sparse signal  $X(k_r)$  for  $M$  multiple sensor, where  $k_r$  is the continuous variable on the real wavenumber domain, is modeled by a group of  $K$ -sparse signals  $X_m(k_r)$ , for  $m = 1, \dots, M$ , sharing a common set of wavenumbers  $\mathcal{M}_{k_r}$ . The wavenumbers are in the continuous wavenumber interval  $\mathbb{K}_r = [k_{r,L}, k_{r,U}]$ , where  $k_{r,U}$  and  $k_{r,L}$  ( $k_{r,L} = k_{r,U} - 2\pi/R_s$ ) are the upper and lower bounds, respectively, of the wavenumber of interest. Given the spatial sampling  $R_s$ , the maximum wavenumber interval is  $2\pi/R_s$ . Then, the group of  $K$ -sparse signals has the form,

$$X_m(k_r) = \sum_{k=1}^K x_{m,k} \delta(k_r - k_{r,k}), \quad m = 1, \dots, M, \quad (5)$$

where  $\delta(k_r - k_{r,k})$  is a Dirac measure at  $k_{r,k}$ . Each  $X_m(k_r)$  shares a set of  $k_{r,k}$  (support), i.e.,  $\mathcal{M}_{k_r} = [k_{r,1}, \dots, k_{r,K}]$  (with  $\mathcal{M}_{k_r} \subset \mathbb{K}_r$ ).

Formulation (4) is expressed in terms of  $X_m(k_r)$  on the continuous wavenumber domain  $\mathbb{K}_r$ ,

$$Y_{m,n} = \int_{\mathbb{K}_r} X_m(k_r) e^{-jk_r r_n} dk_r + E_{m,n}, \\ m = 1, \dots, M, \quad n = 1, \dots, N. \quad (6)$$

The measurement matrix  $\mathbf{Y}$  has the form

$$\mathbf{Y} = [\mathcal{F}_N X_1, \dots, \mathcal{F}_N X_M]^\top + \mathbf{E}, \quad (7)$$

where  $\mathcal{F}_N$  is the linear mapping operator for Fourier transform. It maps the continuous variable  $X_m$  to the  $m$ th row vector of the measurement  $\mathbf{y}_m$ ; i.e.,  $\mathcal{F}_N X_m = [\sum_{k=1}^K x_{m,k} e^{-jk_r k r_1}, \dots, \sum_{k=1}^K x_{m,k} e^{-jk_r k r_N}] \in \mathbb{C}^N$ .

### C. Group TV norm

The TV norm has been introduced as a grid-free measure for imposing sparsity for grid-free CS,<sup>38,39</sup> and the TVNM is a single sensor data processing scheme that uses a single measurement vector as an input. TVNM has been extended to gTVNM to deal with a multiple measurement matrix.<sup>44</sup> Adopting the matrix formulation, each  $X_m(k_r)$ ,  $m = 1, \dots, M$ , is  $K$ -sparse and shares a common support  $\mathcal{M}_{k_r}$ , so that group sparsity is simultaneously imposed over  $M$  sensors. With the continuous wavenumber interval  $\mathbb{K}_r = [k_{r,L}, k_{r,U}]$  in Eq. (6), gTV norm partitions the group of continuous measures  $X_m(k_r)$ ,  $m = 1, \dots, M$ , into a set  $B$  in the wavenumber domain, e.g.,  $B_1 = k_{r,L}$  and  $B_\infty = k_{r,U}$ , determines disjoint measurable components (non-zero components in  $X_m(k_r)$ ), imposes  $l_2$ -norm on each group of  $K$  groups consisting of non-zero components, which share common wave-numbers, and adds the  $l_2$ -norm values,<sup>44</sup>

$$\|X\|_{\text{gTV}} = \sup \sum_{j=1}^{\infty} \|X(B_j)\|_2 = \sup \sum_{j=1}^{\infty} \sqrt{\sum_{m=1}^M |X_m(B_j)|^2}, \quad (8)$$

where the supremum (sup) is taken over the set  $B$  into a finite number of disjoint measurable components. gTV norm is a generalization of the TV norm<sup>50</sup> that derives sum of  $K$  number of  $l_2$ -norm of the amplitudes, which correspond to  $k$ th  $k_r$ , for  $k = 1, \dots, K$ , i.e.,  $\sum_{k=1}^K \sqrt{\sum_{m=1}^M |x_{m,k}|^2}$ . Suppose a matrix  $\mathbf{X} \in \mathbb{C}^{M \times K}$ , which is composed of  $x_{m,k}$  for  $m = 1, \dots, M$  and  $k = 1, \dots, K$ . gTV norm is the continuous analog to the  $l_{1,2}$ -norm of  $\mathbf{X} = [\mathbf{x}_1, \dots, \mathbf{x}_K]$ ,

$$\|X\|_{\text{gTV}} = \sum_{k=1}^K \|\mathbf{x}_k\|_2. \quad (9)$$

### D. Primal problem

With the convex measure, gTV norm, the mode extraction problem is solved using the following gTVNM:

$$\begin{aligned} & \underset{\tilde{X}}{\text{minimize}} && \|\tilde{X}\|_{\text{gTV}} \\ & \text{subject to} && \begin{cases} \mathbf{Y} = [\mathcal{F}_N \tilde{X}_1, \dots, \mathcal{F}_N \tilde{X}_M]^\top + \mathbf{E}, \\ \|\mathbf{E}\|_{\mathcal{F}} \leq \epsilon, \end{cases} \end{aligned} \quad (10)$$

where  $\tilde{X}$  is an estimate of the solution  $X$  and the operator  $\|\mathbf{E}\|_{\mathcal{F}} = \sqrt{\text{trace}(\mathbf{E}\mathbf{E}^\top)}$  is the Frobenius norm.  $\epsilon$  is bounding the noise and determined separately. The noise floor  $\epsilon$  controls the data fitting with respect to the Frobenius norm, i.e.,  $\|\mathbf{Y} - [\mathcal{F}_N \tilde{X}_1, \dots, \mathcal{F}_N \tilde{X}_M]^\top\|_{\mathcal{F}} = \|\mathbf{E}\|_{\mathcal{F}} \leq \epsilon$ , determining the sparsity of the solution. Large  $\epsilon$  permits a large amount of noise with poor data fit, but results in a very sparse solution from the objective of Eq. (10).

Since  $\tilde{X}$  is a continuous variable on the continuous wavenumber domain, it is difficult to solve Eq. (10) directly. To determine support of  $\tilde{X}$ , the primal problem (10) is rescaled as a semi-definite programming (SDP) with finite dimensional variables, and then, estimates the amplitudes.<sup>39,40,44,49</sup> To do so, we use the Lagrangian duality concept<sup>51</sup> to consider the constraints in Eq. (10) by augmenting the objective function using a weighted sum of constraints.

To formulate the dual problem to problem (10), the Lagrangian associated with the problem (10) is constructed by making the explicit equality constraints,  $\mathbf{Y} = [\mathcal{F}_N \tilde{X}_1, \dots, \mathcal{F}_N \tilde{X}_M]^\top + \mathbf{E}$ , and inequality constraints,  $\|\mathbf{E}\|_{\mathcal{F}} \leq \epsilon$ , implicit in the objective function,<sup>51</sup>

$$\begin{aligned} \mathcal{L}(\tilde{X}, \mathbf{C}, \xi) = & \|\tilde{X}\|_{\text{gTV}} + \langle \mathbf{C}, \mathbf{Y} - [\mathcal{F}_N \tilde{X}_1, \dots, \mathcal{F}_N \tilde{X}_M]^\top - \mathbf{E} \rangle \\ & + \xi(\|\mathbf{E}\|_{\mathcal{F}}^2 - \epsilon^2), \end{aligned} \quad (11)$$

where  $\mathbf{C} \in \mathbb{C}^{M \times N}$  is the matrix of the Lagrange dual variables related to the equality constraints,  $\mathbf{Y} = [\mathcal{F}_N \tilde{X}_1, \dots, \mathcal{F}_N \tilde{X}_M]^\top + \mathbf{E}$ ;  $\xi \in \mathbb{R}^+$  are Lagrange dual variables related to the inequality constraints,  $\|\mathbf{E}\|_{\mathcal{F}} \leq \epsilon$ ; and the operator  $\langle \mathbf{C}, \mathbf{Y} \rangle$  is the matrix inner product of  $\mathbf{C}$  and  $\mathbf{Y}$ , i.e.,  $\langle \mathbf{C}, \mathbf{Y} \rangle = \text{trace}(\mathbf{CY}^\top)$ .

### E. Dual problem

The dual problem is defined by maximizing the dual function, which is the infimum of the Lagrangian over the variable of the primal problem.<sup>40,51</sup> Since the primal problem (10) is convex, strong duality holds whereby the location of the primal minimum and the dual maximum are the same. To formulate the dual problem to the problem (10), the dual function  $g(\mathbf{C})$  is the infimum (inf) of the Lagrangian (11) over  $\tilde{X}$ ,<sup>51</sup>

$$\begin{aligned} g(\mathbf{C}, \xi) = & \inf_{\tilde{X}} \mathcal{L}(\tilde{X}, \mathbf{C}, \xi) \\ = & \langle \mathbf{C}, \mathbf{Y} \rangle - \langle \mathbf{C}, \mathbf{E} \rangle + \xi(\|\mathbf{E}\|_{\mathcal{F}}^2 - \epsilon^2) \\ & + \inf_{\tilde{X}} \left( \|\tilde{X}\|_{\text{gTV}} - \sum_{m=1}^M \langle \mathbf{c}_{m,:}, (\mathcal{F}_N \tilde{X}_m) \rangle \right), \end{aligned} \quad (12)$$

where  $\mathbf{c}_{m,:}$  is the  $m$ th row of  $\mathbf{C}$ . Minimizing  $g(\mathbf{C}, \xi)$  over the noise  $\mathbf{E}$  and maximizing  $g(\mathbf{C}, \xi)$  over the Lagrange multiplier related to the inequality constraint  $\xi$ ,

$$\begin{aligned}\frac{\partial g(\mathbf{C}, \xi)}{\partial \mathbf{E}} &= -\mathbf{C} + 2\xi \mathbf{E} = \mathbf{0}, \\ \frac{\partial g(\mathbf{C}, \xi)}{\partial \xi} &= \|\mathbf{E}\|_{\mathcal{F}}^2 - \epsilon^2 = 0,\end{aligned}\quad (13)$$

whereby  $\mathbf{E} = \mathbf{C}/(2\xi) = \epsilon \mathbf{C}/\|\mathbf{C}\|_{\mathcal{F}}$  (since  $4\xi^2 = \|\mathbf{C}\|_{\mathcal{F}}^2/\|\mathbf{E}\|_{\mathcal{F}}^2 = \|\mathbf{C}\|_{\mathcal{F}}^2/\epsilon^2$ ). Then, the dual function (12) for the optimal values,  $\mathbf{E}_{\text{opt}}$  and  $\xi_{\text{opt}}$ , becomes

$$\begin{aligned}g(\mathbf{C})|_{\mathbf{E}_{\text{opt}}, \xi_{\text{opt}}} &= \langle \mathbf{C}, \mathbf{Y} \rangle - \epsilon \|\mathbf{C}\|_{\mathcal{F}} \\ &\quad + \inf_{\tilde{X}} \left( \|\tilde{X}\|_{\text{gTV}} - \sum_{m=1}^M \langle \mathbf{c}_{m:}, (\mathcal{F}_N \tilde{X}_m) \rangle \right) \\ &= \langle \mathbf{C}, \mathbf{Y} \rangle - \epsilon \|\mathbf{C}\|_{\mathcal{F}} \\ &\quad + \inf_{\tilde{X}} \left( \|\tilde{X}\|_{\text{gTV}} - \sum_{m=1}^M \langle \mathcal{F}_N^H \mathbf{c}_{m:}, \tilde{X}_m \rangle \right) \\ &= \langle \mathbf{C}, \mathbf{Y} \rangle - \epsilon \|\mathbf{C}\|_{\mathcal{F}} \\ &\quad + \inf_{\tilde{X}} \left( \sup \sum_{j=1}^{\infty} \sqrt{\sum_{m=1}^M |\tilde{X}_m(B_j)|^2} \right. \\ &\quad \left. - \sup \sum_{j=1}^{\infty} \sum_{m=1}^M (\mathcal{F}_N^H \mathbf{c}_{m:}(B_j))^H \tilde{X}_m(B_j) \right).\end{aligned}\quad (14)$$

The infimum term in Eq. (14) is trivial  $-\infty$ , unless  $\sum_{m=1}^M |\mathcal{F}_N^H \mathbf{c}_{m:}(k_r)|^2 \leq 1$  for all  $k_r$ . Therefore, the dual function  $g(\mathbf{C})$  is

$$g(\mathbf{C}) = \begin{cases} \langle \mathbf{C}, \mathbf{Y} \rangle - \epsilon \|\mathbf{C}\|_{\mathcal{F}}, & \sup_{k_r} \sum_{m=1}^M |\mathcal{F}_N^H \mathbf{c}_{m:}(k_r)|^2 \leq 1, \\ -\infty, & \text{otherwise.} \end{cases}\quad (15)$$

The Lagrange dual problem of Eq. (10) is formulated by maximizing the dual function  $g(\mathbf{C})$ ,

$$\begin{aligned}&\underset{\mathbf{C}}{\text{maximize}} \quad \langle \mathbf{C}, \mathbf{Y} \rangle - \epsilon \|\mathbf{C}\|_{\mathcal{F}} \\ &\text{subject to} \quad \sup_{k_r} \sum_{m=1}^M |\mathcal{F}_N^H \mathbf{c}_{m:}(k_r)|^2 \leq 1.\end{aligned}\quad (16)$$

According to Proposition 2.4 of Ref. 44, the dual problem is recast as SDP,

$$\begin{aligned}&\underset{\mathbf{C}}{\text{maximize}} \quad \langle \mathbf{C}, \mathbf{Y} \rangle - \epsilon \|\mathbf{C}\|_{\mathcal{F}} \\ &\text{subject to} \quad \begin{bmatrix} \mathbf{Q} & \mathbf{C}^H \\ \mathbf{C} & \mathbf{I}_M \end{bmatrix} \succeq 0, \\ &\sum_{i=1}^{N-j} Q_{i,i+j} = \begin{cases} 1, & j = 0 \\ 0, & j = 1, \dots, N-1, \end{cases}\end{aligned}\quad (17)$$

where  $\mathbf{I}_M$  is the identity matrix of size  $M$  and “ $\succeq$ ” denotes positive semi-definite. The SDP (17) can be solved by

efficient SDP solvers.<sup>52–54</sup> Herein, we utilize the CVX program<sup>55</sup> to solve Eq. (17).

The SDP (17) is solved over  $(M+N)^2/2$  number of variables, given by the positive semi-definite constraints. Thus, the problem with continuous parameter (10) is solved over the finite dimensional program (17).

## F. Mode wavenumber estimation

The detection of the support of  $X$  indicates the mode wavenumbers. Strong duality guarantees that by locating the maximum of the dual problem (16), or equivalently Eq. (17), we obtain the minimum of the primal problem (10).<sup>40</sup> Using the Lagrange dual solution  $\mathbf{C}$  obtained from Eq. (17), the detection of the support  $\mathcal{M}_{k_r}$  of the primal solution  $\tilde{X}$  can be performed by support locating through the dual polynomial.<sup>44</sup> The support  $\mathcal{M}_{k_r}$  is related to the maximum modulus of the trigonometric polynomial, which is obtained from the dual solution  $\mathbf{C}$ , Eq. (17),<sup>44</sup>

$$\mathcal{Q}(k_r) = \sum_{m=1}^M |\mathcal{F}_N^H \mathbf{c}_{m:}(k_r)|^2,\quad (18)$$

which is the dual polynomial. From Lemma 3.5 of Ref. 44, the support  $\mathcal{M}_{k_r}$  is determined by finding points where the dual polynomial becomes one, i.e.,  $\mathcal{M}_{k_r} = \{k_r | \mathcal{Q}(k_r) = 1\}$ . The mathematical theorems and proofs underlying the gTVNM method are confirmed by Ref. 44.

## G. Mode shape estimation

The amplitude at the support  $\mathcal{M}_{k_r}$  of the primal solution  $\tilde{X}$  indicates the mode amplitudes at each sensor, and thus mode shapes  $\Psi_k$ , for  $k = 1, \dots, K$ . Consider the determined support of  $X$ ,  $\mathcal{M}_{k_r} = [k_{r,1}, \dots, k_{r,K}]$ , the relation between the support and the measurement  $\mathbf{Y}$  in Eq. (4), and the relation between the amplitudes of  $X$  and the  $k$ th mode amplitude at the  $m$ th sensor of the VLA,  $x_{m,k} = Q\Psi_k(z_s)\Psi_{k,m}/\sqrt{k_{r,k}}$ . In absence of noise, from Eq. (4), the measurement matrix  $\mathbf{Y}$  is related to a set of unnormalized mode shapes  $\hat{\Psi} = [\hat{\Psi}_1, \dots, \hat{\Psi}_K] \in \mathbb{C}^{M \times K}$ , whose  $(m,k)$ -element is  $Q\Psi_k(z_s)\Psi_{k,m}$ ,

$$\mathbf{Y}^T = \mathbf{A}_{\mathcal{M}_{k_r}} \hat{\Psi}^T,\quad (19)$$

where  $\mathbf{A}_{\mathcal{M}_{k_r}}$  is an  $(N \times K)$ -matrix, whose  $(n,k)$ -element is  $e^{-jk_{r,k}f_n}/\sqrt{k_{r,k}}$  for  $k_{r,k} \in \mathcal{M}_{k_r}$ . Then, the amplitudes of the unnormalized mode shapes are recovered from

$$\Psi^T = \mathbf{A}_{\mathcal{M}_{k_r}}^\dagger \mathbf{Y}^T,\quad (20)$$

where  $\mathbf{A}_{\mathcal{M}_{k_r}}^\dagger$  denotes the pseudoinverse of  $\mathbf{A}_{\mathcal{M}_{k_r}}$ .

## H. Grid-free CS techniques

Grid-free CS employs two major techniques, TV norm based algorithms<sup>39,44</sup> and atomic norm minimization (ANM),<sup>38,45</sup> and both techniques can be applied to the grid-free CS mode extraction. TVNM utilizes TV norm, which is defined on the sparse signal  $X$ . ANM utilizes atomic norm,

which is defined on the noiseless measurement  $\mathbf{Y}$ , which is composed of sparse signal atoms.

In the ANM framework, the measurement matrix  $\mathbf{Y}$  (6) becomes

$$\mathbf{Y} = \sum_{k=1}^K \hat{x}_k \mathbf{b}_k \mathbf{a}(k_{r,k})^\top + \mathbf{E} = \sum_{k=1}^K \hat{x}_k \mathbf{A}(k_{r,k}, \mathbf{b}_k) + \mathbf{E}, \quad (21)$$

where  $\hat{x}_k = \sqrt{\sum_{m=1}^M |x_{m,k}|^2}$ ,  $b_{m,k} = x_{m,k}/\hat{x}_k$  with  $\|\mathbf{b}_k\|_2 = 1$ , and  $\mathbf{a}(k_{r,k}) = [e^{-jk_{r,k}r_1}, \dots, e^{-jk_{r,k}r_N}]^\top \in \mathbb{C}^N$ . An atom that represents the noiseless measurement matrix  $\tilde{\mathbf{Y}}$  is defined as  $\mathbf{A}(k_r, \mathbf{b}) = \mathbf{b}\mathbf{a}(k_r)^\top$ , where  $k_r \in [k_{r,L}, k_{r,U}]$ ,  $\mathbf{b} \in \mathbb{C}^M$  with  $\|\mathbf{b}\|_2 = 1$ . The infinite set  $\mathcal{A}$  forms a set of atoms for  $\tilde{\mathbf{Y}}$ , and is defined as

$$\mathcal{A} = \{\mathbf{A}(k_r, \mathbf{b}) | k_r \in [k_{r,L}, k_{r,U}], \|\mathbf{b}\|_2 = 1\}. \quad (22)$$

The atomic norm of  $\tilde{\mathbf{Y}}$  is defined by finding a unit ball with the convex hull of  $\mathcal{A}$ ,

$$\begin{aligned} \|\tilde{\mathbf{Y}}\|_{\mathcal{A}} &= \inf \{s > 0 \mid \tilde{\mathbf{Y}} \in s \text{conv}(\mathcal{A})\} \\ &= \inf \left\{ \sum_{k=1}^K \hat{x}_k \mid \tilde{\mathbf{Y}} = \sum_{k=1}^K \hat{x}_k \mathbf{A}(k_{r,k}, \mathbf{b}_k), \hat{x}_k > 0 \right\}. \end{aligned} \quad (23)$$

TV norm and atomic norm are defined differently, but both techniques are equivalent because they have the same results,

$$\|X\|_{g\text{TV}} = \|\tilde{\mathbf{Y}}\|_{\mathcal{A}} = \sum_{k=1}^K \hat{x}_k. \quad (24)$$

The difference between the two techniques is TVNM utilizes the Lagrange dual problem (16) of the primal problem, recasts the Lagrange dual problem as SDP, and solves the SDP (17) of the Lagrange dual problem. However, ANM recasts its primal problem as SDP, solves the SDP of the primal problem, and utilizes the Lagrange dual concept of the primal problem to obtain the support, which makes up the measurement. The ANM problem has the primal problem as

$$\underset{\tilde{\mathbf{Y}}}{\text{minimize}} \quad \|\tilde{\mathbf{Y}}\|_{\mathcal{A}} + \frac{\tau}{2} \|\mathbf{Y} - \tilde{\mathbf{Y}}\|_{\mathcal{F}}^2, \quad (25)$$

where the regularization parameter  $\tau$  controls the balance between the sparsity and the data fitting. The SDP of the primal problem (25) is provided by Theorem 1 of Ref. 45,

$$\begin{aligned} \underset{\mathbf{u}, \tilde{\mathbf{Y}}, \mathbf{Z}}{\text{minimize}} \quad & \frac{1}{2M} \text{trace}(\text{Toep}(\mathbf{u})) + \frac{1}{2} \text{trace}(\mathbf{Z}) + \frac{\tau}{2} \|\mathbf{Y} - \tilde{\mathbf{Y}}\|_{\mathcal{F}}^2 \\ \text{subject to} \quad & \begin{bmatrix} \text{Toep}(\mathbf{u}) & \tilde{\mathbf{Y}}^\top \\ \tilde{\mathbf{Y}} & \mathbf{Z} \end{bmatrix} \succeq 0, \end{aligned} \quad (26)$$

where  $\text{Toep}(\mathbf{u}) \in \mathbb{C}^{N \times N}$  denotes the Toeplitz matrix whose first row is equal to  $\mathbf{u} \in \mathbb{C}^N$ . The Toeplitz matrix satisfies the following property:<sup>47</sup>

$$\text{Toep}(\mathbf{u}) = \sum_{k=1}^K \hat{x}_k \mathbf{a}(k_{r,k}) \mathbf{a}(k_{r,k})^\top, \quad (27)$$

and  $\mathbf{Z}$  is a free variable to be optimized, satisfying  $\text{trace}(\text{Toep}(\mathbf{u}))/2M + \text{trace}(\mathbf{Z})/2 = \sum_{k=1}^K \hat{x}_k$ . Both SDPs, Eqs. (17) and (26), deal with the same size matrix,  $(M+N) \times (M+N)$ , and have similar computational complexity.

In addition, TVNM finds the support by locating where the dual polynomial is one, but ANM requires decomposition of the Toeplitz matrix (27), e.g., Vandermonde decomposition, to find the support. However, ANM can use the same support detection method as TVNM by using CVX<sup>55</sup> because CVX directly returns the dual solution in the process of solving the primal problem of ANM.

### III. SIMULATION RESULTS

#### A. Isovelocity problem

The simplest case is the isovelocity profile with constant density and boundary conditions with a pressure-release surface and a rigid bottom at depth  $D$ . The mode  $k$  horizontal wavenumber is given by Eq. (5.46) of Ref. 1,

$$k_{c,k}(\omega_0) = \sqrt{\left(\frac{\omega_0}{c}\right)^2 - \left[\left(k - \frac{1}{2}\right)\frac{\pi}{D}\right]^2}, \quad (28)$$

where to assure a real wavenumber  $k < (\omega_0 D / \pi c) + 1/2$ , i.e.,  $k_{c,k} = k_{r,k}$ . The corresponding mode  $k$  shape is given by

$$\Psi_k(\omega_0, z_n) = \sqrt{\frac{2\rho}{D}} \sin\left(\left(k - \frac{1}{2}\right)\frac{\pi}{D} z_n\right). \quad (29)$$

Consider a source of frequency  $\omega_0 = 200\pi$  rad/s ( $f = 100$  Hz) at  $z_s = 20$  m in a  $D = 100$  m deep waveguide with sound speed  $c = 1500$  m/s and density  $\rho = 1000$  kg/m<sup>3</sup>. In this case, there are 13 propagating modes of which the first 4 are considered, i.e.,  $k_{r,k}$ ,  $k = 1, \dots, 4$ , and their mode shapes are plotted in Fig. 2(c). The  $M = 49$  array has uniform intersensor spacing 2 m and spans the entire water column (from 2 to 98 m). The  $N = 25$  sampling ranges span 1–5.8 km with the sampling range interval  $R_s = 200$  m.

As for the mode wavenumber estimation, the classic way to estimate the wavenumber is computing the wavenumber spectrum  $\hat{S}$  using the discrete Fourier transform of the pressure field (3),

$$\hat{S}(k_r, z_m) = \mathbf{p}_{m,:}^\top e^{j\mathbf{k}k_r}, \quad (30)$$

where  $\mathbf{p}_{m,:}^\top$  is the  $m$ th row of  $\mathbf{P}$ . Figure 2(a) shows the wavenumber spectrum for  $N = 400$  (ranges spanning 1–80.8 km) and  $N = 25$  (ranges spanning 1–5.8 km), both with  $z_m = 50$  m depth and  $R_s = 200$  m. The dual polynomial attains unit magnitude, i.e.,  $\mathcal{Q}(k_r) = 1$ , at each corresponding mode wavenumber [Fig. 2(b)]. The sizes of the mainlobes and the number of corresponding sidelobes are determined by  $N$  and  $R_s$  for both the wavenumber spectrum and the dual polynomial. The difference is that each mode component has a different amplitude for the wavenumber spectrum, but the dual

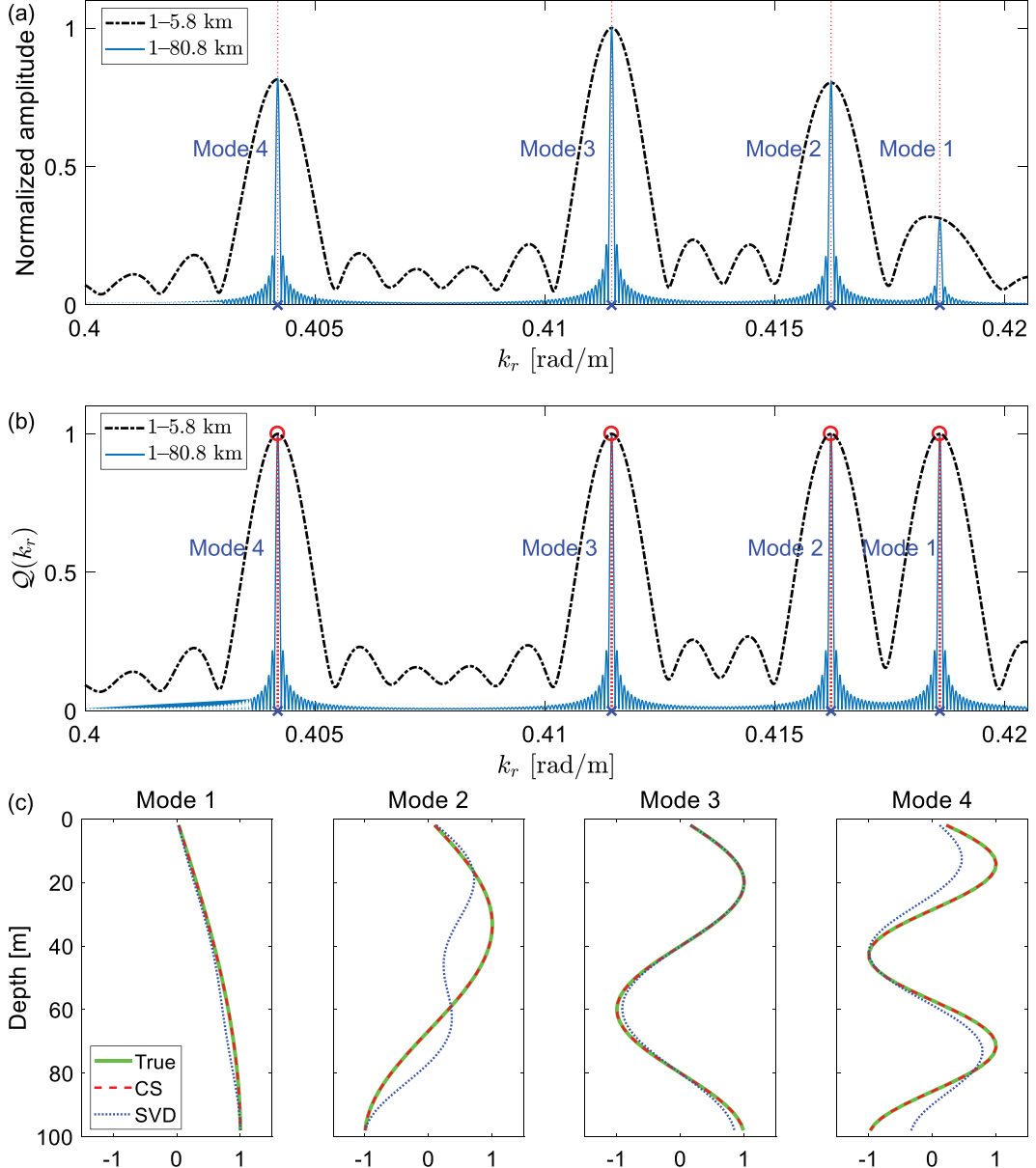


FIG. 2. (Color online) (a) Wavenumber spectrum and (b) dual polynomial and the points at which it is one ( $\circ$ ), with 1–80.8 km case (solid) and 1–5.8 km case (dashed-dotted). The true mode wavenumbers ( $\times$ ) are at  $k_r = [0.4186, 0.4162, 0.4114, 0.4042]$  rad/m. (c) Mode shape reconstruction with grid-free CS (dashed) and SVD (dotted), as well as the true mode shapes (solid). Mode amplitudes are normalized to maximum amplitude of one.

polynomial has unit amplitudes, Eq. (18). In addition, the sidelobes of each mode affect other modes in the wavenumber spectrum, whereas the dual polynomial does not. Once the mode wavenumbers are estimated, the corresponding mode shapes are computed as in Fig. 2(c). For the 1–80.8 km case, the grid-free CS results show excellent performance, while SVD offers poor results for some modes because the mode functions are not orthonormal.

Next, we consider the coherent mode shape case where the mode shapes have a high coherence,  $\langle \Psi_i, \Psi_j \rangle$  for  $i \neq j$ .  $\langle \Psi_i, \Psi_j \rangle \approx 0$  for  $i \neq j$ , if the array densely spans the entire water column.  $\langle \Psi_i, \Psi_j \rangle \approx 1$  for  $i \neq j$ , if the array spans a narrow partial water column, which has similar mode shapes as in Fig. 3. The  $M=20$  array has intersensor spacing 1 m and spans the partial water column (from 1 to 20 m). Four modes have high coherence values and violate the orthonormal

condition. Grid-free CS offers accurate estimates for both mode wavenumbers and the corresponding mode shapes.

## B. SWellEx-96 simulation

The acoustic field in a 216.5 m depth range-independent ocean was simulated using the Kraken normal mode model.<sup>56</sup> The field, generated by a 49 Hz source at 54 m depth, was sampled at  $N=30$  sampling ranges spanning 1–5.35 km with the sampling range interval  $R_s = 150$  m and  $M = 64$  evenly spaced VLA elements spanning 94.125–212.25 m depth with intersensor spacing 1.875 m. The sound speed profile and bottom structure were adopted from the shallow water evaluation cell experiment 1996 (SWellEx-96) Event S5<sup>6</sup> (Fig. 4). The field shows six propagating modes as in Figs. 5 and 6.

Figure 5 shows the mode extraction results of grid-free CS and SVD using simulation data from the SWellEx-96

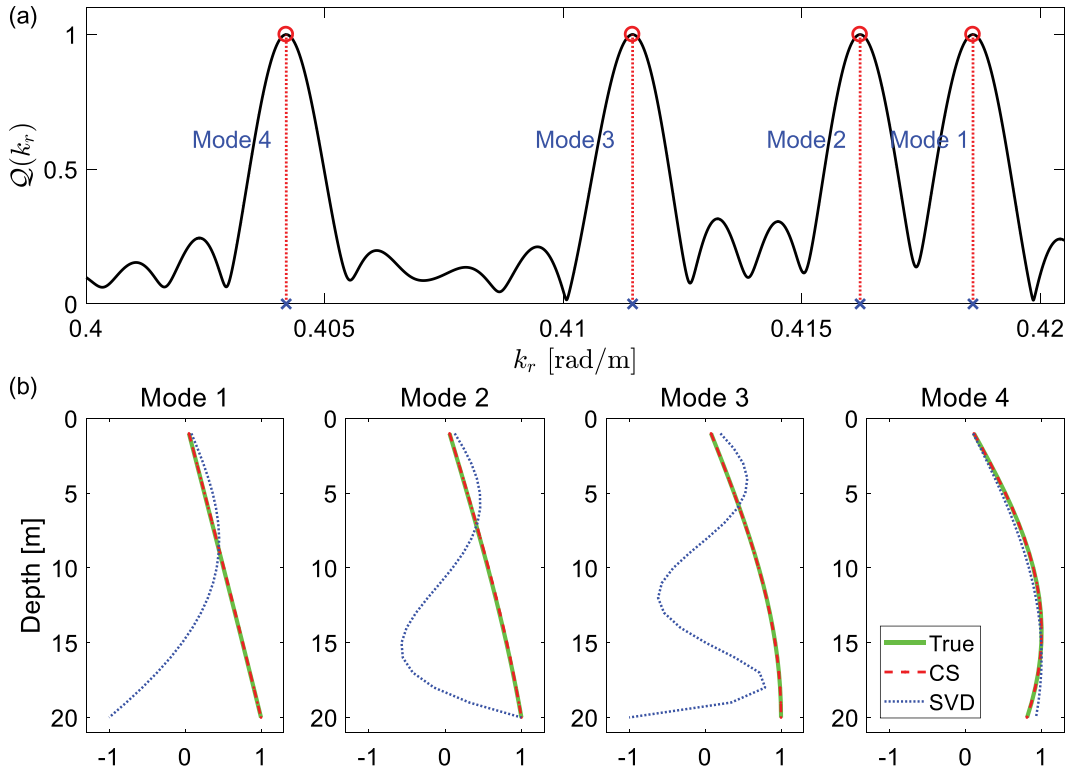


FIG. 3. (Color online) Same as Fig. 2, but with a partial water column spanning array (from 1 to 20 m depth with 1 m interval).

experimental configuration. SVD is degraded significantly due to the partial water column spanning array that violates the orthogonality condition. However, grid-free CS offers good reconstruction for both mode wavenumbers and corresponding mode shapes.

We consider the mode extraction problem using the same data as Fig. 5, but when the mode wavenumbers are complex valued (Fig. 6). In this case, we assume that the modes propagate to fairly long ranges, i.e.,  $k_{r,k} \gg k_{i,k}$ . Although the mode wavenumbers are complex valued, because the imaginary parts are much smaller than the real parts, grid-free CS returns accurate estimates. However, because grid-free CS can find only real-valued wavenumbers, Table I, it cannot perfectly recover the complex-valued mode wavenumbers and their mode shapes.

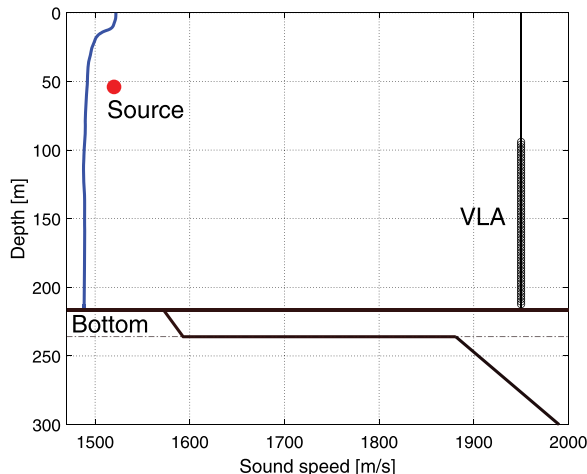


FIG. 4. (Color online) Schematic of the SWellEx-96 environment.

The grid-free CS can estimate the mode wavenumbers and the corresponding mode amplitudes using only single  $M=1$  sensor data. We consider the same environment as Fig. 5. The six propagating modes have the full water column spanning shapes as shown in Fig. 7(a). In this case, single sensor data processing uses a single measurement vector, one row of the measurement matrix  $\mathbf{Y}$ , as the input, so the problem in the grid-free CS manner becomes the TVNM problem, which is a single measurement vector processing scheme. From the single sensor data processing, the mode wavenumbers are obtained from support detection of a sparse signal [Figs. 7(b)–7(f)]. For each case, the single sensor cases at five different depths [red dotted lines in Fig. 7(a)] are considered. Note that, except Fig. 7(b), the mode amplitude of one of six modes is zero: mode 3 in Fig. 7(c), mode 4 in Fig. 7(d), mode 5 in Fig. 7(e), and mode 6 in Fig. 7(f). Even with a single sensor data, grid-free CS offers good reconstruction for mode wavenumbers as in Fig. 7(b). However, if the sensor depth coincides with where the mode amplitude is zero, grid-free CS fails to reconstruct the corresponding mode wavenumber [Figs. 7(c)–7(f)]. Even if grid-free CS can offer good reconstruction with single sensor data (TVNM), a multiple sensor data processing scheme (gTVNM) is required to overcome the problem of missing the mode wavenumbers whose mode amplitudes coincide with the zero-crossing points. Also, with a sufficient number of measurements, gTVNM improves support detection performance.<sup>44,49</sup>

We present the importance of a good choice of the sampling range interval  $R_s$  and the number of range samples  $N$  in Fig. 8. The sampling range interval  $R_s$  is related to the size of the wavenumber search space, i.e.,  $k_r \in [(k_{r,U} - 2\pi/R_s), k_{r,U}]$ . The upper bound of the wavenumber is determined by

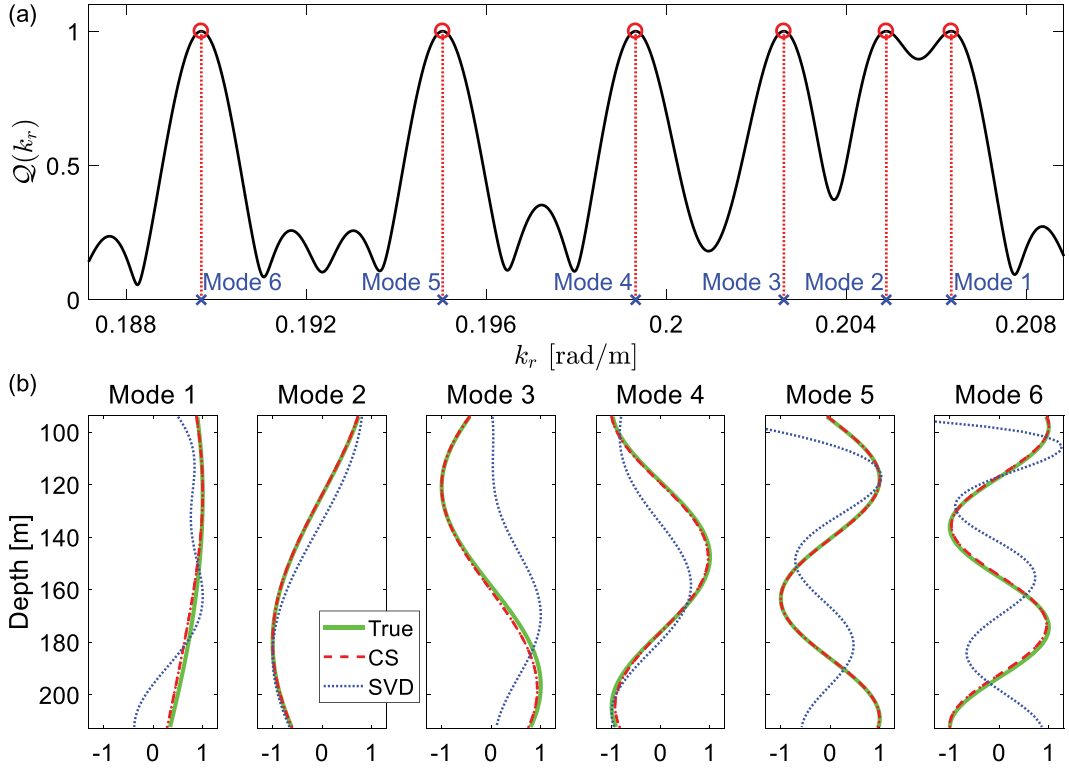


FIG. 5. (Color online) Same as Fig. 2, except for the environment of the problem. The true mode wavenumbers ( $\times$ ) are at  $k_r = [0.2063, 0.2049, 0.2026, 0.1993, 0.1950, 0.1897]$  rad/m.

the minimum sound speed, i.e.,  $k_{r,U} = \omega_0/c_{\min}$ . A large  $R_s$  invokes a narrow search space, e.g.,  $R_s = 400$  m corresponds to the search space,  $k_r \in [0.1913, 0.2070]$  rad/m. In this case, grid-free CS cannot estimate the sixth mode which has

$k_r = 0.1897$  rad/m. To obtain a sufficiently broad wavenumber search space, a small  $R_s$  is needed. On the other hand, a small  $R_s$  can hamper grid-free CS from reconstructing the mode wavenumber accurately. Figure 8 shows the mode

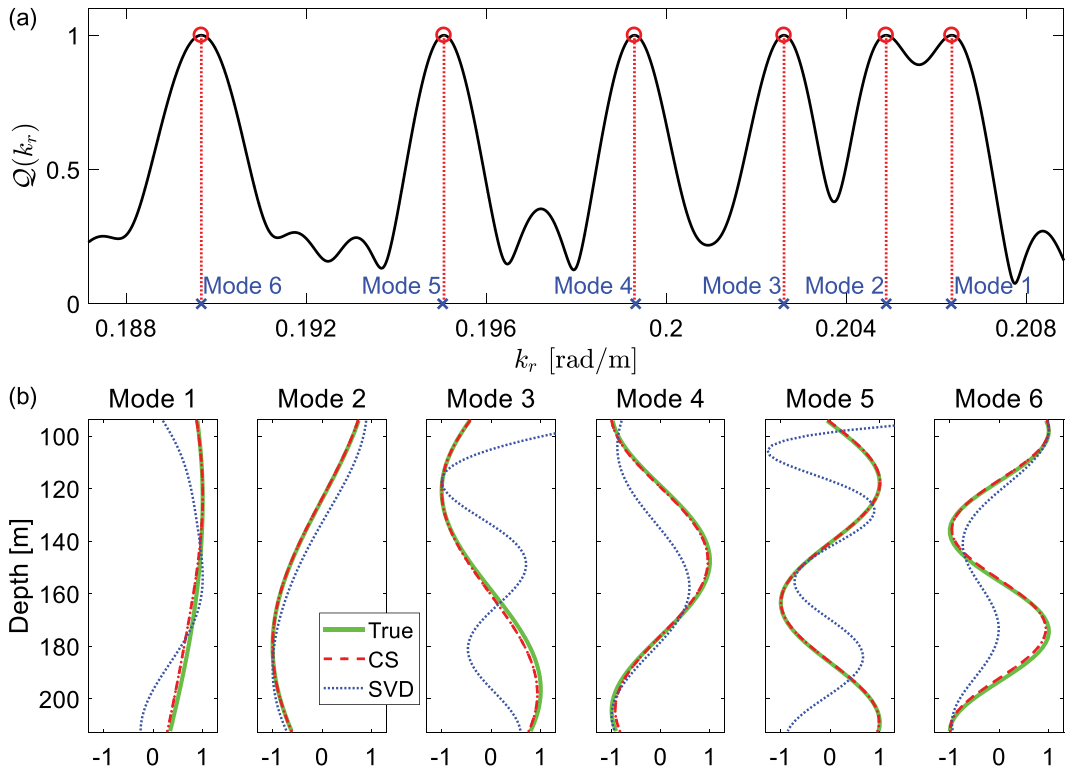


FIG. 6. (Color online) Same as Fig. 5, except that the mode wavenumbers are complex-valued.

TABLE I. The mode wavenumbers in Fig. 6.

	True $k_r - jk_i$	Grid-free CS
Mode 1	0.2063 – 0.000004j	0.2063
Mode 2	0.2049 – 0.00014j	0.2049
Mode 3	0.2026 – 0.000025j	0.2026
Mode 4	0.1993 – 0.000039j	0.1993
Mode 5	0.1950 – 0.000057j	0.1950
Mode 6	0.1896 – 0.000089j	0.1896

wavenumber extraction results using  $R_s = 150$  m and  $R_s = 75$  m. In Fig. 8(b), the dual polynomial  $Q(k_r)$  suffers from low resolution and merges several peaks that are closely located, so that grid-free CS cannot offer good reconstruction. To overcome this problem, many range samples  $N$  can be used. Figure 8(c) employs a larger value of  $N = 60$  than that of Figs. 8(a) and 8(b) ( $N = 30$ ). However, the use of many range samples leads to a high computational time, and higher modes can be attenuated through long range transmission. A small  $R_s$  and a large  $N$  provides accurate reconstruction to grid-free CS. In the case of limited  $N$ , grid-free CS needs as large as possible  $R_s$  under a condition where the tightened search space, accompanied by larger  $R_s$ , to cover all of the wavenumbers of interest.

### C. Robust normal mode extraction of gTVNM based grid-free CS in the presence of noise

In the presence of noise, gTVNM based grid-free CS offers robust estimates for both mode wavenumbers and the corresponding mode shapes. We consider the mode extraction problem using the same environment as Fig. 6, but in the presence of noise with the signal-to-noise ratio (SNR = 6 dB). The SNR is defined as

$$\text{SNR} = 20 \log_{10} \left( \frac{\|\mathcal{F}_N X_m\|_2}{\|\mathbf{e}_{m:}\|_2} \right), \quad m = 1, \dots, M, \quad (31)$$

where  $\mathcal{F}_N X_m \in \mathbb{C}^N$  is the  $m$ th row of the noiseless measurement and  $\mathbf{e}_{m:}$  is the  $m$ th row of the additive Gaussian noise  $\mathbf{E} \in \mathbb{C}^{M \times N}$ .

Similar to the mode wavenumber estimation in Fig. 7, from single sensor data processing, the estimated mode wavenumbers using grid-free CS (TVNM) and the wavenumber spectrum computed using Eq. (30) are obtained, as shown in Fig. 9(a). The estimated wavenumbers with TVNM fluctuate at the vicinity of the true wavenumbers due to noise. The wavenumber spectrum has low amplitudes and TVNM fails to estimate wavenumbers where mode amplitudes coincide with the zero-crossing points. For this reason, it cannot be proper to utilize TVNM on each sensor data independently and then average the obtained wavenumbers.

Next, we consider multiple sensor data processing with grid-free CS (gTVNM), on-grid CS, and wavenumber spectrum, as shown in Fig. 9(b). To consider multiple sensor data, wavenumber spectra of different sensor data (different depths) are averaged as follows:

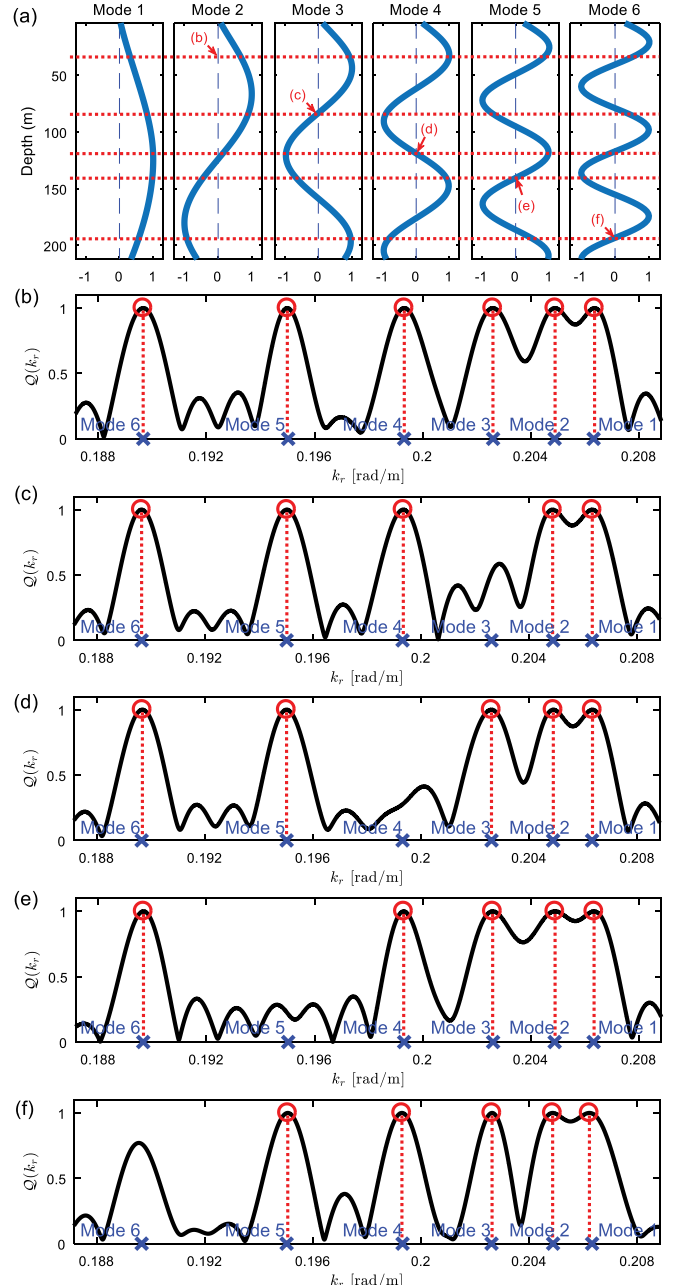


FIG. 7. (Color online) Mode wavenumber reconstruction results using single sensor data with grid-free CS. (a) The full water column spanning mode shapes in the same environment as Fig. 5. (b)–(f) Dual polynomial and the points at which it is one (○).

$$\hat{S}_{\text{multi}}(k_r) = \frac{1}{M} \sum_{m=1}^M |\hat{S}(k_r, z_m)| = \frac{1}{M} \sum_{m=1}^M |\mathbf{p}_{m:}^\top e^{jk_r}|. \quad (32)$$

On-grid CS estimates mode wavenumbers and the corresponding mode shapes with the following formulation:

$$\begin{aligned} & \text{minimize}_{\hat{\Psi}_{\text{on-grid}}} \|\hat{\Psi}_{\text{on-grid}}^\top\|_{2,1} \\ & \text{subject to } \|\mathbf{Y}^\top - \mathbf{A}_{\tilde{M}_{k_r}} \hat{\Psi}_{\text{on-grid}}^\top\|_{\mathcal{F}} \leq \epsilon_{\text{on-grid}}, \end{aligned} \quad (33)$$

where  $\hat{\Psi}_{\text{on-grid}}$  is a set of unnormalized mode shapes,  $N_{\text{grid}}$  is the number of grid points of the on-grid CS scheme,

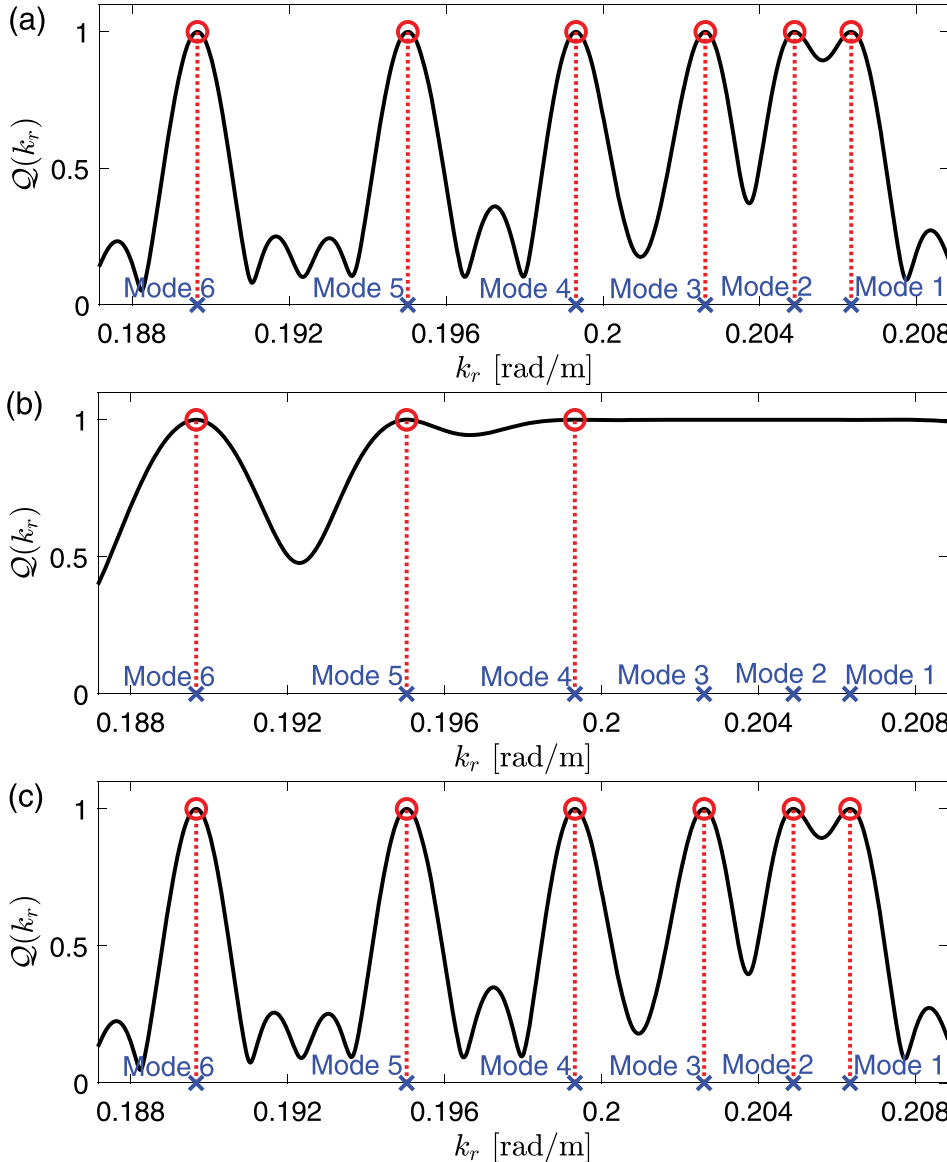


FIG. 8. (Color online) Same as Fig. 6, except for (a)  $N = 30$  and  $R_s = 150$  m, (b)  $N = 30$  and  $R_s = 75$  m, and (c)  $N = 60$  and  $R_s = 75$  m.

$\tilde{\mathcal{M}}_{k_r} = [\tilde{k}_{r,1}, \dots, \tilde{k}_{r,N_{\text{grid}}}]$  (e.g.,  $\tilde{k}_{r,1} = k_{r,L}$  and  $\tilde{k}_{r,N_{\text{grid}}} = k_{r,U}$ ), and  $\mathbf{A}_{\tilde{\mathcal{M}}_{k_r}}$  is an  $(N \times N_{\text{grid}})$ -matrix, whose  $(n, n_{\text{grid}})$ -element is  $e^{-jk_{r,n_{\text{grid}}} r_n} / \sqrt{\tilde{k}_{r,n_{\text{grid}}}}$  for  $\tilde{k}_{r,n_{\text{grid}}} \in \tilde{\mathcal{M}}_{k_r}$ . Here, we divided the wavenumber interval  $[k_{r,L}, k_{r,U}]$  into 1000 uniform grids.

We have chosen the noise floor  $\epsilon_{\text{on-grid}}$  to make a sparsity level of the on-grid CS of seven (the truth is six). The on-grid CS fails to estimate modes 4 and 5, and estimates mode 1 with poor amplitude. At the vicinity of the wavenumbers of modes 2, 3, and 6, the estimated wavenumbers with on-grid CS show neighboring two components, which is due to the basis mismatch.

In the presence of noise, the reconstructed mode shapes with grid-free CS, on-grid CS, and SVD are obtained, as shown in Fig. 9(c). As for the on-grid CS, where the basis mismatch occurs, we have taken the closest component to the true wavenumbers between neighboring two components. The obtained wavenumbers with on-grid CS are located closely to the true points, and the corresponding computed mode shapes look similar to the obtained mode shapes with the grid-free CS. gTVNM based grid-free CS

offers robust reconstruction for both mode wavenumbers and the corresponding mode shapes in the presence of noise.

#### IV. EXPERIMENTAL RESULTS

In this section, grid-free CS mode extraction is applied to the experimental data. The data set is from the SWellEx-96 experiment Event S5 recorded on a  $M = 64$  VLA spanning 94.125–212.25 m depth. During the Event S5, from 23:15–00:30 on 10–11 May 1996 near San Diego, CA, two sources, a shallow source and a deep source, were towed simultaneously from 8.65 km southwest to 2.90 km northeast of the VLA. Each source transmitted a unique set of tones, and, particularly, the deep source was transmitting 13 narrowband frequencies. Here, we focus on the deep source towed at 54 m depth, especially its 49 Hz frequency component among the 13 submitted frequencies.

The range samples spanning from 1.120 to 5.116 km with sampling range interval  $R_s = 4$  m ( $N = 1000$ ) is utilized. To get different ranges of samples with this data set, we used the global positioning system (GPS) data to synchronize the

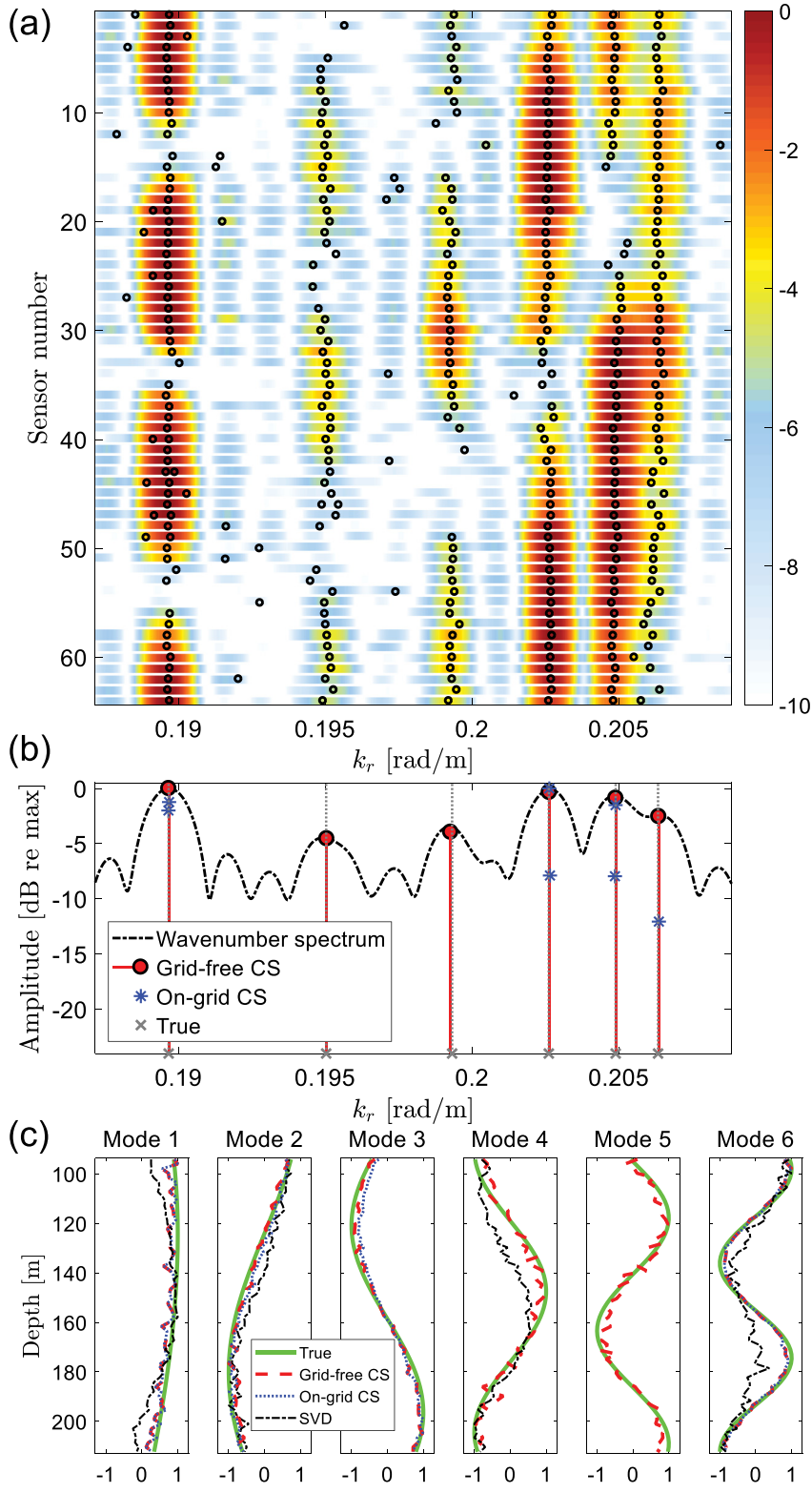


FIG. 9. (Color online) Same as Fig. 6, except that the measurements are contaminated with noise (SNR = 6 dB). (a) Mode wavenumber reconstruction results using single sensor data with grid-free CS (○) and wavenumber spectrum (background). (b) Mode wavenumber reconstruction results using multiple sensor data with grid-free CS (○), on-grid CS (\*), and wavenumber spectrum (dashed-dotted), and (c) the corresponding mode shapes reconstruction with grid-free CS (dashed), on-grid CS (dotted), SVD (dashed-dotted), and the true mode shapes (solid).

range of interest and the corresponding time, assuming that there is no uncertainty on the range. The processed recording to get a range sample has a duration of 2.7 s ( $2^{12}$  samples), and we assume that the range between the source and the VLA is stationary for the duration.

The grid-free CS mode extraction scheme is formally configured with different ranges of samples between source and VLA in the experimental setup using a fixed source and a fixed VLA. However, the experimental data involve a

moving source and a fixed VLA. The source motion leads to Doppler broadening of the mode wavenumber spectrum because Doppler effect scatters the mode wavenumber components around the true wavenumbers.<sup>19</sup> The mode wavenumber spectrum in real data processing with a moving source is sensitive to the data processing scheme or errors in the estimation of the Doppler shift.<sup>19,57</sup> Since the mode wavenumber estimation with a moving source and a fixed VLA was not a primary goal in this paper, we utilize simple

assumptions so there are several sources for discrepancies in wavenumber estimation due to the assumptions. Here, we assume that the source moves toward VLA with uniform radial motion (constant radial velocity  $v_s$ ), mode wavenumbers are shifted solely by the Doppler effect and the corresponding mode shapes remain constant.

Let us recall the exponential term in Eq. (2) and the time-frequency Fourier transform pair, Eq. (1), then the exponent resulting from the Doppler shift has the form<sup>19</sup>  $j(\omega_0 t - [\tilde{k}_{r,m} \{1/(1+v_s/\tilde{u}_m)\} r])$ , where  $\tilde{k}_{r,m}$  is Doppler shifted mode  $m$  wavenumber and  $\tilde{u}_m$  is the Doppler shifted mode  $m$  group velocity. Assuming frequency shift  $\omega_D$  of the measurement is caused by only the Doppler shifted spatiotemporal properties of the mode  $m$  field contribution  $\tilde{k}_{r,m}$ , and each mode  $m$  field is affected by the same Doppler shift contribution ( $v_s/\tilde{u}_m \ll 1$ ), i.e.,  $v_s/\tilde{u}_m = v_s/\bar{u}$ , where  $\bar{u}$  is the group velocity averaged over the  $m$  modes, we have expressed the Doppler shifted exponent as  $j(\omega_0 t - [\tilde{k}_{r,m} \{1/(1+v_s/\bar{u})\} r]) \approx j(\omega_0 t - [\tilde{k}_{r,m} \{1/(1+v_s/\bar{u})\} r]) = j(\omega_0 t + \omega_D t - k_{r,m} r)$ . We utilize the measurement for processing by correcting the Doppler shift using  $e^{-j\omega_D t_n} \tilde{p}(r_n, z, \omega_0 + \omega_D)$ ,<sup>57</sup> where  $\tilde{p}(r_n, z, \omega_0 + \omega_D)$  is the Doppler shifted measured pressure and  $t_n$  is time at range  $r_n$ .

The grid-free CS estimates the mode wavenumbers and mode shapes using the SWellEx-96 data. Kraken normal mode model simulation using the SWellEx-96 environment shows six modes. We have chosen the noise floor to make a sparsity level of the grid-free CS of eight. Despite the simple assumptions, the grid-free CS locates six modes around the Kraken mode wavenumbers as shown in Fig. 10. Grid-free CS provides higher resolution than the Fourier transform based wavenumber spectrum that CS is capable of resolving closely located wavenumbers.

Using the estimated mode wavenumbers in Fig. 10, the corresponding mode shapes are calculated by Eq. (20). However, since unknown conditions in real data are unavoidable, the pseudoinverse did not show definite mode shapes. It is likely that the pseudoinverse solution can become a better fit to the data but potentially follows the noise too closely.

Given a sound speed profile, which is collected using CTD, we recall the shooting method<sup>1</sup> as a solution to the original depth-separated wave equation. This provides us with the finite difference representation of the differential equation, given by Eq. (5.141) of Ref. 1,

$$\begin{aligned} \hat{\Psi}_{\text{shoot}}(z_{i+1}, k_r) &= -\hat{\Psi}_{\text{shoot}}(z_{i-1}, k_r) \\ &+ \left\{ 2 - \delta_z^2 \left[ \frac{\omega^2}{c^2(z_i)} - k_r^2 \right] \right\} \\ &\times \hat{\Psi}_{\text{shoot}}(z_i, k_r), \end{aligned} \quad (34)$$

where  $\hat{\Psi}_{\text{shoot}}(z, k_r)$  are the mode shapes calculated from the shooting method,  $i$  is an index over depth,  $\delta_z$  is the depth interval, and  $c(z)$  is depth-dependent sound speed.

Using the estimated wavenumbers in Fig. 10, given  $c(z)$  and two initial values [we use  $\hat{\Psi}_{\text{shoot}}(z_0, k_r) = 0$  and  $\hat{\Psi}_{\text{shoot}}(z_1, k_r) = 1$ ], the mode shapes of the shooting method,  $\hat{\Psi}_{\text{shoot}} \in \mathbb{R}^{M \times K}$ , can be calculated. Assuming the perturbations

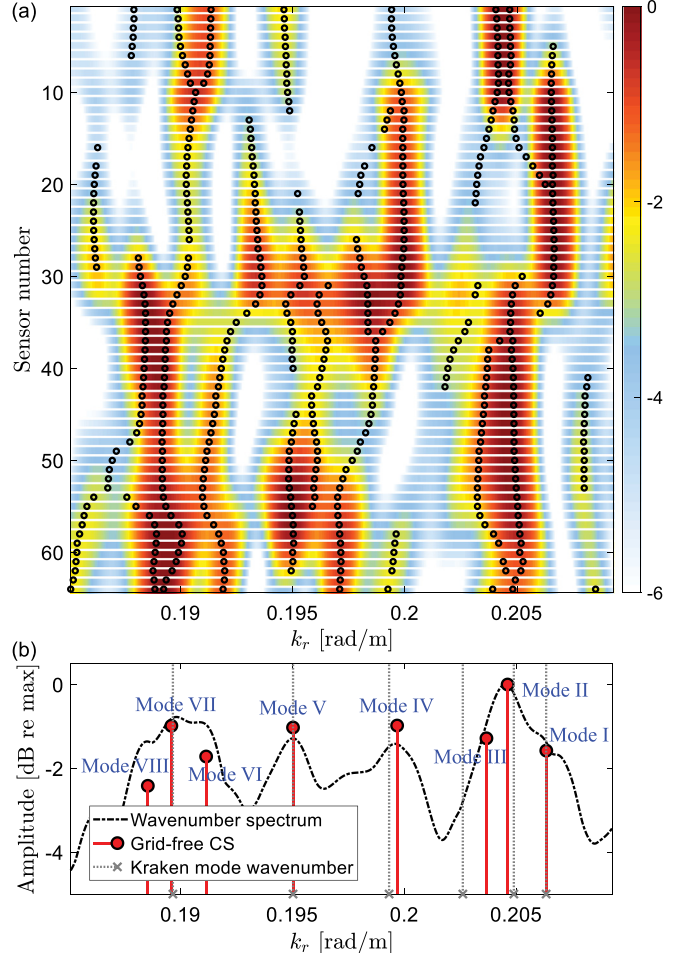


FIG. 10. (Color online) (a) Mode wavenumber reconstruction with experimental data using single sensor data with grid-free CS ( $\circ$ ) and wavenumber spectrum (background). (b) Mode wavenumber reconstruction with experimental data using multiple sensor data with grid-free CS ( $\circ$ ) and wavenumber spectrum (dashed-dotted).

$\mathbf{D} \in \mathbb{R}^{M \times K}$  to the reference mode shapes are small, the unnormalized mode shapes  $\hat{\Psi}$  are recovered from

$$\hat{\Psi} = \hat{\Psi}_{\text{shoot}} + \mathbf{D}, \quad (35)$$

where

$$\begin{aligned} \mathbf{D}(\lambda) = \underset{\mathbf{D}}{\text{minimize}} \quad & \left\| \mathbf{Y}^T - \mathbf{A}_{\mathcal{M}_{k_r}} (\hat{\Psi}_{\text{shoot}}^T + \mathbf{D}^T) \right\|_{\mathcal{F}}^2 \\ & + \lambda \|\mathbf{D}\|_{\mathcal{F}}^2, \end{aligned} \quad (36)$$

where  $\mathbf{A}_{\mathcal{M}_{k_r}}$  is an  $(N \times K)$ -matrix, whose  $(n,k)$ -element is  $e^{-jk_{r,k}r_n}/\sqrt{k_{r,k}}$  for  $k_{r,k} \in \mathcal{M}_{k_r}$ .  $\lambda$  controls the relative importance of the solution energy and the measurement fit.

The grid-free CS shows eight mode shapes and SVD shows only four mode shapes, as shown in Fig. 11. Note that SVD cannot extract the mode wavenumbers, and in the process of mode shape extraction, the orthonormality condition is not satisfied.

## V. CONCLUSION

This paper is concerned with the extraction of the normal modes of acoustic propagation in the ocean waveguide

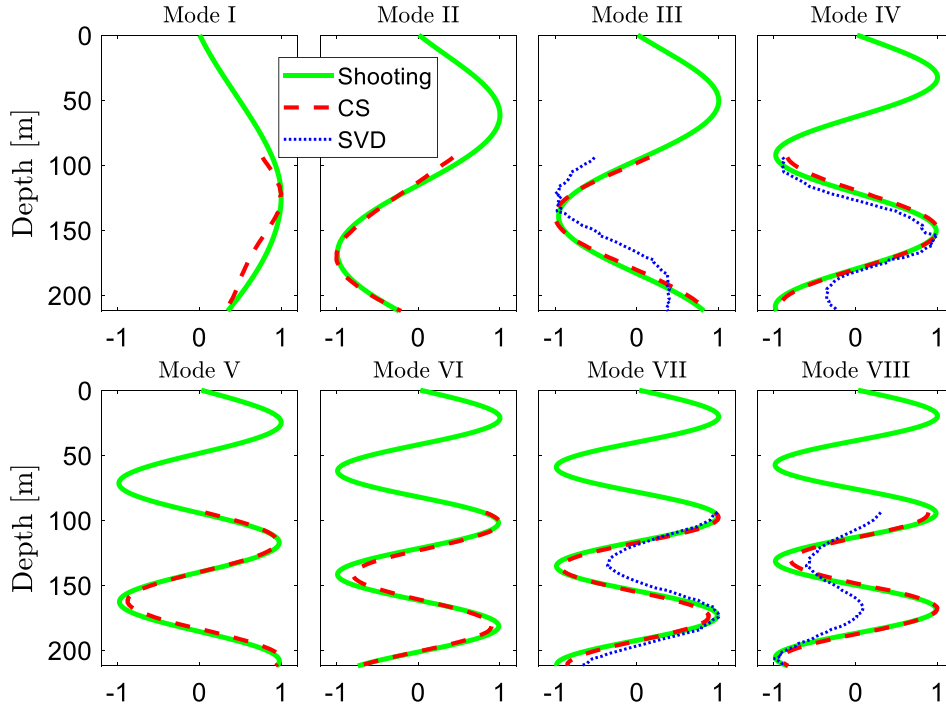


FIG. 11. (Color online) Mode shape reconstruction with experimental data using grid-free CS (dashed) and SVD (dotted). The reference mode shapes (solid) are calculated using shooting method with the estimated wavenumbers in Fig. 10.

from VLA data. We estimate the mode wavenumbers and corresponding mode shapes via grid-free CS.

First, CS is applied to take advantage of the sparse nature in which finite discrete modes describe the propagation of underwater sound. Grid-free CS assures that discretization of the wavenumber search grid in the conventional CS is avoided. Moreover, development of the multiple measurement processing improves performance in estimation over the single measurement processing.

In contrast to the established SVD method, grid-free CS provides both mode wavenumbers and mode shapes. Grid-free CS provides accurate estimation results even with a partial water column spanning array data, as well as when the mode shapes do not satisfy the orthogonality condition. The real data example indicates that the grid-free CS mode extraction is capable of estimating the mode horizontal wavenumbers and corresponding mode shapes.

## ACKNOWLEDGMENTS

This research was supported by the Office of Naval Research Grant No. N00014-18-1-2118 and the Agency for Defense Development in the Republic of Korea under Contract No. UD160015DD.

## APPENDIX: SVD MODE EXTRACTION

The SVD of an  $M \times N$  complex matrix  $\mathbf{A}$  is

$$\mathbf{A} = \mathbf{U}\Sigma\mathbf{V}^H, \quad (\text{A1})$$

where  $\Sigma$  is a diagonal matrix whose elements are the positive singular values of  $\mathbf{A}$  in order from largest to smallest down the diagonal. The columns of both  $\mathbf{U}$  and  $\mathbf{V}$  satisfy the orthonormality condition

$$\mathbf{U}^H\mathbf{U} = \mathbf{U}\mathbf{U}^H = \mathbf{I}_M, \quad \mathbf{V}^H\mathbf{V} = \mathbf{V}\mathbf{V}^H = \mathbf{I}_N. \quad (\text{A2})$$

For noiseless data, the data covariance matrix  $\mathbf{C} \in \mathbb{C}^{M \times M}$  is formulated by the outer product of the pressure field  $\mathbf{P}$  in Eq. (3),

$$\begin{aligned} \mathbf{C} &= \frac{1}{N} \mathbf{P} \mathbf{P}^H, \\ C_{m,n} &= \sum_{p,q=1}^{M,M} \Psi_p(z_m) \Psi_q^H(z_n) \lambda_{p,q}, \\ m &= 1, \dots, M, \quad n = 1, \dots, M, \end{aligned} \quad (\text{A3})$$

where

$$\lambda_{p,q} = \frac{2\pi S^2 \Psi_p(z_s) \Psi_q(z_s)}{N \rho^2(z_s) \sqrt{k_{r,p} k_{r,q}}} \sum_{n=1}^N \frac{e^{-jk_{r,pq} r_n}}{r_n}, \quad (\text{A4})$$

$$k_{r,pq} \equiv k_{r,p} - k_{r,q}. \quad (\text{A5})$$

SVD mode extraction assumes that Eq. (A3) has the approximation

$$\mathbf{C} \approx \hat{\Psi} \Lambda \hat{\Psi}^H, \quad (\text{A6})$$

where the columns of  $\hat{\Psi} \in \mathbb{C}^{M \times M}$  satisfy the orthonormality condition

$$\hat{\Psi}^H \hat{\Psi} = \hat{\Psi} \hat{\Psi}^H = \mathbf{I}_M, \quad (\text{A7})$$

and the first  $K$  columns (modes) of  $\hat{\Psi}$  are made up of  $\{\hat{\psi}_1, \dots, \hat{\psi}_K\}$ , and

$$\Lambda_{m,n} = \lambda_{m,n}, \quad (\text{A8})$$

with  $\Lambda_{m,n} = 0$  for  $m \neq n$  and  $\Lambda_{m,m} = 0$  for  $m = K + 1, \dots, M$ . This approximation needs  $\{\hat{\psi}_1, \dots, \hat{\psi}_K\}$  to be orthogonal to each other and the off-diagonal components of  $\Lambda$  to be zeroes. The true modes satisfy the condition

$$\int_0^H \Psi_m(z) \Psi_n(z) dz = \delta_{mn}, \quad (\text{A9})$$

where  $H$  is the depth where the modes decay to zero amplitude, often deep in the sediment, and  $\delta$  denotes a Kronecker delta. Thus, Eq. (A7) is only valid for densely sampled modes all the way to  $H$ . The off-diagonal components of  $\mathbf{A}$  approach zero when  $\text{Re}(k_{r,mn})(r_N - r_1)/2\pi$  is large.<sup>17</sup>

Comparing Eq. (A6) to Eq. (A1) shows the relation between the matrices  $\mathbf{U}$  and  $\mathbf{V}$  and the matrix  $\Psi$ , which contains the mode shapes. Finally, SVD mode extraction applies SVD to the data SCM and extracts mode shapes from a set of orthonormal eigenvectors, which correspond to the singular values.

- <sup>1</sup>F. B. Jensen, W. A. Kuperman, M. B. Porter, and H. Schmidt, *Computational Ocean Acoustics*, 2nd ed. (Springer, New York, 2011), pp. 337–455.
- <sup>2</sup>N. E. Collison and S. E. Dosso, “Regularized matched-mode processing for source localization,” *J. Acoust. Soc. Am.* **107**(6), 3089–3100 (2000).
- <sup>3</sup>K. Kim, W. Seong, and K. Lee, “Adaptive surface interference suppression for matched-mode source localization,” *IEEE J. Ocean. Eng.* **35**(1), 120–130 (2010).
- <sup>4</sup>T. C. Yang, “Data-based matched-mode source localization for a moving source,” *J. Acoust. Soc. Am.* **135**(3), 1218–1230 (2014).
- <sup>5</sup>A. B. Baggeroer, W. A. Kuperman, and P. N. Mikhalevsky, “An overview of matched field methods in ocean acoustics,” *IEEE J. Ocean. Eng.* **18**(4), 401–424 (1993).
- <sup>6</sup>N. O. Booth, P. A. Baxley, J. Rice, P. Schey, W. Hodgkiss, G. D’Spain, and J. Murray, “Source localization with broad-band matched-field processing in shallow water,” *IEEE J. Ocean. Eng.* **21**(4), 402–412 (1996).
- <sup>7</sup>H. Song, S. Kim, W. Hodgkiss, and W. Kuperman, “Environmentally adaptive reverberation nulling using a time reversal mirror,” *J. Acoust. Soc. Am.* **116**(2), 762–768 (2004).
- <sup>8</sup>S. Walker, P. Roux, and W. Kuperman, “Focal depth shifting of a time reversal mirror in a range-independent waveguide,” *J. Acoust. Soc. Am.* **118**(3), 1341–1347 (2005).
- <sup>9</sup>T. L. Poole, G. V. Frisk, J. F. Lynch, and A. D. Pierce, “Geoacoustic inversion by mode amplitude perturbation,” *J. Acoust. Soc. Am.* **123**(2), 667–678 (2008).
- <sup>10</sup>J. Bonnel, C. Gervaise, B. Nicolas, and J. Mars, “Single-receiver geoacoustic inversion using modal reversal,” *J. Acoust. Soc. Am.* **131**(1), 119–128 (2012).
- <sup>11</sup>E. Shang and Y. Wang, “Tomographic inversion of the El Niño profile by using a matched-mode processing (MMP) method,” *IEEE J. Ocean. Eng.* **19**(2), 208–213 (1994).
- <sup>12</sup>M. S. Ballard, G. V. Frisk, and K. M. Becker, “Estimates of the temporal and spatial variability of ocean sound speed on the New Jersey shelf,” *J. Acoust. Soc. Am.* **135**(6), 3316–3326 (2014).
- <sup>13</sup>J. Bonnel, A. M. Thode, S. B. Blackwell, K. Kim, and A. Michael Macrander, “Range estimation of bowhead whale (*Balaena mysticetus*) calls in the Arctic using a single hydrophone,” *J. Acoust. Soc. Am.* **136**(1), 145–155 (2014).
- <sup>14</sup>R. H. Ferris, “Comparison of measured and calculated normal-mode amplitude functions for acoustic waves in shallow water,” *J. Acoust. Soc. Am.* **52**(3B), 981–989 (1972).
- <sup>15</sup>J. R. Buck, J. C. Preisig, and K. E. Wage, “A unified framework for mode filtering and the maximum *a posteriori* mode filter,” *J. Acoust. Soc. Am.* **103**(4), 1813–1824 (1998).
- <sup>16</sup>P. Hursky, W. S. Hodgkiss, and W. A. Kuperman, “Matched field processing with data-derived modes,” *J. Acoust. Soc. Am.* **109**(4), 1355–1366 (2001).
- <sup>17</sup>T. B. Neilsen and E. K. Westwood, “Extraction of acoustic normal mode depth functions using vertical line array data,” *J. Acoust. Soc. Am.* **111**(2), 748–756 (2002).
- <sup>18</sup>S. Walker, P. Roux, and W. Kuperman, “Data-based mode extraction with a partial water column spanning array,” *J. Acoust. Soc. Am.* **118**(3), 1518–1525 (2005).
- <sup>19</sup>S. Walker, P. Roux, and W. A. Kuperman, “Modal Doppler theory of an arbitrarily accelerating continuous-wave source applied to mode extraction in the oceanic waveguide,” *J. Acoust. Soc. Am.* **122**(3), 1426–1439 (2007).
- <sup>20</sup>J. Bonnel, C. Gervaise, P. Roux, B. Nicolas, and J. Mars, “Modal depth function estimation using time-frequency analysis,” *J. Acoust. Soc. Am.* **130**(1), 61–71 (2011).
- <sup>21</sup>J. Bonnel, S. Caporale, and A. Thode, “Waveguide mode amplitude estimation using warping and phase compensation,” *J. Acoust. Soc. Am.* **141**(3), 2243–2255 (2017).
- <sup>22</sup>A. Drémeau, F. Le Courtois, and J. Bonnel, “Reconstruction of dispersion curves in the frequency-wavenumber domain using compressed sensing on a random array,” *IEEE J. Ocean. Eng.* **42**(4), 914–922 (2017).
- <sup>23</sup>E. J. Candès and M. B. Wakin, “An introduction to compressive sampling,” *IEEE Signal Process. Mag.* **25**(2), 21–30 (2008).
- <sup>24</sup>M. Elad, *Sparse and Redundant Representations: From Theory to Applications in Signal and Image Processing* (Springer, New York, 2010), pp. 1–359.
- <sup>25</sup>P. Gerstoft, C. F. Mecklenbräuker, W. Seong, and M. Bianco, “Introduction to compressive sensing in acoustics,” *J. Acoust. Soc. Am.* **143**, 3731–3736 (2018).
- <sup>26</sup>A. Xenaki, P. Gerstoft, and K. Mosegaard, “Compressive beamforming,” *J. Acoust. Soc. Am.* **136**(1), 260–271 (2014).
- <sup>27</sup>P. Gerstoft, A. Xenaki, and C. F. Mecklenbräuker, “Multiple and single snapshot compressive beamforming,” *J. Acoust. Soc. Am.* **138**(4), 2003–2014 (2015).
- <sup>28</sup>P. Gerstoft, C. F. Mecklenbräuker, A. Xenaki, and S. Nannuru, “Multisnapshot sparse Bayesian learning for DOA,” *IEEE Signal Process. Lett.* **23**(10), 1469–1473 (2016).
- <sup>29</sup>M. Bianco and P. Gerstoft, “Compressive acoustic sound speed profile estimation,” *J. Acoust. Soc. Am.* **139**(3), EL90–EL94 (2016).
- <sup>30</sup>K. L. Gemba, W. S. Hodgkiss, and P. Gerstoft, “Adaptive and compressive matched field processing,” *J. Acoust. Soc. Am.* **141**(1), 92–103 (2017).
- <sup>31</sup>Y. Choo and W. Seong, “Compressive spherical beamforming for localization of incipient tip vortex cavitation,” *J. Acoust. Soc. Am.* **140**(6), 4085–4090 (2016).
- <sup>32</sup>F. Le Courtois and J. Bonnel, “Compressed sensing for wideband wavenumber tracking in dispersive shallow water,” *J. Acoust. Soc. Am.* **138**(2), 575–583 (2015).
- <sup>33</sup>J. B. Harley and J. M. Moura, “Sparse recovery of the multimodal and dispersive characteristics of Lamb waves,” *J. Acoust. Soc. Am.* **133**(5), 2732–2745 (2013).
- <sup>34</sup>J. B. Harley and J. M. Moura, “Dispersion curve recovery with orthogonal matching pursuit,” *J. Acoust. Soc. Am.* **137**(1), EL1–EL7 (2015).
- <sup>35</sup>Z. Li, H. Niu, Z. Gong, and R. Zhang, “Sparse Bayesian learning for horizontal wavenumber retrieval in underwater acoustical signal processing,” in *2018 23rd International Conference on Digital Signal Processing (DSP)*, IEEE, Shanghai, China (2018), pp. 1–4.
- <sup>36</sup>Y. Chi, L. L. Scharf, A. Pezeshki, and A. R. Calderbank, “Sensitivity to basis mismatch in compressed sensing,” *IEEE Trans. Signal Process.* **59**(5), 2182–2195 (2011).
- <sup>37</sup>D. H. Chae, P. Sadeghi, and R. A. Kennedy, “Effects of basis-mismatch in compressive sampling of continuous sinusoidal signals,” in *Proceedings of the 2nd International Conference on Future Computer and Communication (ICFCC)*, IEEE, Wuhan, China (2010), Vol. 2, pp. 739–743.
- <sup>38</sup>G. Tang, B. N. Bhaskar, P. Shah, and B. Recht, “Compressed sensing off the grid,” *IEEE Trans. Inf. Theory* **59**(11), 7465–7490 (2013).
- <sup>39</sup>E. J. Candès and C. Fernandez-Granda, “Towards a mathematical theory of super-resolution,” *Comm. Pure Appl. Math.* **67**(6), 906–956 (2014).
- <sup>40</sup>A. Xenaki and P. Gerstoft, “Grid-free compressive beamforming,” *J. Acoust. Soc. Am.* **137**(4), 1923–1935 (2015).
- <sup>41</sup>Y. Park, W. Seong, and Y. Choo, “Compressive time delay estimation off the grid,” *J. Acoust. Soc. Am.* **141**(6), EL585–EL591 (2017).
- <sup>42</sup>Y. Yang, Z. Chu, Z. Xu, and G. Ping, “Two-dimensional grid-free compressive beamforming,” *J. Acoust. Soc. Am.* **142**(2), 618–629 (2017).
- <sup>43</sup>Y. Yang, Z. Chu, G. Ping, and Z. Xu, “Resolution enhancement of two-dimensional grid-free compressive beamforming,” *J. Acoust. Soc. Am.* **143**(6), 3860–3872 (2018).
- <sup>44</sup>C. Fernandez-Granda, “Super-resolution of point sources via convex programming,” *Inf. Inference* **5**(3), 251–303 (2016).
- <sup>45</sup>Y. Li and Y. Chi, “Off-the-grid line spectrum denoising and estimation with multiple measurement vectors,” *IEEE Trans. Signal Process.* **64**(5), 1257–1269 (2016).
- <sup>46</sup>Z. Yang, J. Li, P. Stoica, and L. Xie, “Sparse methods for direction-of-arrival estimation,” [arXiv.org/abs/1609.09596](https://arxiv.org/abs/1609.09596) (2016).

- <sup>47</sup>C. Steffens, M. Pesavento, and M. E. Pfetsch, “A compact formulation for the  $l_{2,1}$  mixed-norm minimization problem,” *IEEE Trans. Signal Process.* **66**(6), 1483–1497 (2018).
- <sup>48</sup>S. Li, D. Yang, G. Tang, and M. B. Wakin, “Atomic norm minimization for modal analysis from random and compressed samples,” [arXiv.org/abs/1703.00938](https://arxiv.org/abs/1703.00938) (2017).
- <sup>49</sup>Y. Park, Y. Choo, and W. Seong, “Multiple snapshot grid free compressive beamforming,” *J. Acoust. Soc. Am.* **143**(6), 3849–3859 (2018).
- <sup>50</sup>W. Rudin, *Real and Complex Analysis*, 3rd ed. (McGraw-Hill, New York, 1987), pp. 116–134.
- <sup>51</sup>S. Boyd and L. Vandenberghe, *Convex Optimization* (Cambridge University Press, New York, 2004), pp. 215–288.
- <sup>52</sup>R. H. Tütüncü, K. C. Toh, and M. J. Todd, “Solving semidefinite-quadratic-linear programs using SDPT3,” *Math. Program.* **95**(2), 189–217 (2003).
- <sup>53</sup>J. F. Sturm, “Using SeDuMi 1.02, a MATLAB toolbox for optimization over symmetric cones,” *Optim. Methods Softw.* **11**(1-4), 625–653 (1999).
- <sup>54</sup>J. Lofberg, “YALMIP: A toolbox for modeling and optimization in MATLAB,” in *2004 IEEE International Conference on Robotics and Automation*, IEEE, New Orleans, LA (2004), pp. 284–289.
- <sup>55</sup>M. Grant, S. Boyd, and Y. Ye, “CVX: MATLAB software for disciplined convex programming (version 2.1) [computer program]” (2008), available at <http://cvxr.com/cvx> (Last viewed June 14, 2018).
- <sup>56</sup>M. B. Porter, “The KRAKEN normal mode program” (SACLANT Undersea Research Centre, La Spezia, Italy, 1991).
- <sup>57</sup>T. C. Yang, “Source depth estimation based on synthetic aperture beamfoming for a moving source,” *J. Acoust. Soc. Am.* **138**(3), 1678–1686 (2015).